Monthly Notices of the ROYAL ASTRONOMICAL SOCIETY

MNRAS **546,** 1–22 (2026) https://doi.org/10.1093/mnras/staf2023
Advance Access publication 2026 January 06

REBELS-IFU: evidence for metal-rich massive galaxies at $z \sim 6-8$

Lucie E. Rowland [1]★ Mauro Stefanon,[2,3] Rychard Bouwens,[1] Jacqueline Hodge,[1] Hiddo Algera [4,5,6] Rebecca Fisher [7] Pratika Dayal [8,9,10,11] Andrea Pallottini [12,13] Daniel P. Stark,[14] Kasper E. Heintz [15,16,17] Manuel Aravena,[18,19] Rebecca A. A. Bowler [7] Karin Cescon,[1] Ryan Endsley [20] Andrea Ferrara,[12] Yoshinobu Fudamoto,[21] Valentino Gonzalez,[22] Luca Graziani,[23,24,25] Cindy Gulis,[26] Thomas Herard-Demanche [1] Hanae Inami [5] Andrès Laza-Ramos,[2,3] Ivana van Leeuwen [1] Ilse de Looze,[27] Themiya Nanayakkara [28] Pascal Oesch [16,17] Katherine Ormerod [29] Marco Palla,[30,31] Nina S. Sartorio [27] Sander Schouws,[1] Renske Smit,[29] Laura Sommovigo [32] Sune Toft,[15,16] John R. Weaver [33] and Paul van der Werf[1]

Affiliations are listed at the end of the paper

Accepted 2025 October 21. Received 2025 July 28; in original form 2025 January 17

ABSTRACT

Metallicity is a crucial tracer of galaxy evolution, providing insights into gas accretion, star formation, and feedback. At high redshift, these processes reveal how early galaxies assembled and enriched their interstellar medium. In this work, we present rest-frame optical spectroscopy of 12 massive ($\log(M_*/\mathrm{M}_\odot) > 9$) galaxies at $z \sim 6$–8 from the Reionization Era Bright Emission Line Survey (REBELS) Atacama Large Millimetre/submillimetre Array (ALMA) large program, observed with the James Webb Space Telescope (*JWST*) NIRSpec integral field unit spectroscopy in the prism mode. These observations span emission lines from [O II]$\lambda\lambda$3727,9 to [S II]$\lambda\lambda$6716,31, providing key information on nebular dust attenuation, ionization states, and chemical abundances. We find lower O32 ratios (average ~ 3.7) and [O III]λ5007 equivalent widths (median $\mathrm{EW}_{[\mathrm{O\,III}]} \sim 480$ Å) than are generally found in existing large spectroscopic surveys at $z > 6$, indicating less extreme ionizing conditions. Strong-line diagnostics suggest that these systems are some of the most metal-rich galaxies observed at $z > 6$ (average $Z_{\mathrm{gas}} \sim 0.4 Z_\odot$), including sources with near-solar oxygen abundances, in line with their high stellar masses (average $\log M_*/\mathrm{M}_\odot \sim 9.5$). Supplementing with literature sources at lower masses, we investigate the mass–metallicity and fundamental metallicity relations (MZR and FMR, respectively) over a 4 dex stellar mass range at $6 < z < 8$. In contrast to recent studies of lower mass galaxies, we find no evidence for negative offsets to the $z = 0$ FMR for the REBELS galaxies. This work demonstrates the existence of chemically enriched galaxies just ~ 1 Gyr after the big bang, and indicates that the MZR is already in place at these early times, in agreement with other recent $z > 3$ studies.

Key words: galaxies: evolution – galaxies: high-redshift – galaxies: ISM.

1 INTRODUCTION

Understanding the formation and evolution of galaxies in the early Universe is a central goal of modern astrophysics. Over the past decade, remarkable progress has been made in extending the redshift frontier, with the highest redshift galaxy observations advancing from $z = 8.68$, achieved by an Lyα detection with Keck/MOSFIRE (Multi-Object Spectrometer for Infra-Red Exploration) in 2015 (A. Zitrin et al. 2015; G. W. Roberts-Borsani et al. 2016), to $z = 14.18$ in 2024 with the *James Webb Space Telescope (JWST)* and the Atacama Large Millimetre/submillimetre Array (ALMA; S. Carniani et al. 2024; S. Schouws et al. 2025) – just ∼300 Myr after the big bang. With *JWST* significantly increasing the number of observed galaxies at $z \gtrsim 10$ (e.g. A. J. Bunker et al. 2023; B. E. Robertson et al. 2023; M. Curti et al. 2024; S. Carniani et al. 2024), studies have uncovered an unexpected population of luminous ($M_{\mathrm{UV}} < -20$) galaxies already in place at these early cosmic times (e.g. M. Castellano et al. 2022; R. P. Naidu et al. 2022; J. A. Zavala et al. 2025; C. M. Casey et al. 2024). Even before *JWST*, there were notable discoveries of massive galaxies (M. L. Strandet et al. 2017; $M_* \sim 10^9$–$10^{11}\mathrm{M}_\odot$, e.g. E. Bañados et al. 2018; D. P. Marrone et al. 2018; R. J. Bouwens et al. 2022) and substantial dust reservoirs (D. Watson et al. 2015; Y. Tamura et al. 2019; H. Inami et al. 2022; S. Schouws et al. 2022) at slightly later cosmic times ($z \sim 6$–8). These observations provide valuable insights into the early assembly of galaxies, but many of these studies lack robust constraints on the metallicity of the systems.

★ E-mail: lrowland@strw.leidenuniv.nl

Metallicity is a key diagnostic for understanding how galaxies have formed and evolved. Metals provide insights into a galaxy's star formation history (SFH), gas inflows and outflows, and the feedback processes that regulate its growth (e.g. R. Maiolino & F. Mannucci 2019). Inflows bring in pristine gas from the surrounding intergalactic medium (IGM) that, while diluting metallicity in the short term, fuels future star formation. This gas eventually forms stars, where nuclear fusion transforms hydrogen and helium into heavier elements. Massive, newly formed stars return energy and metals to the interstellar medium (ISM), and can drive powerful outflows that carry gas and metals out of the galaxy. These expelled metals can escape the galaxy's gravitational pull to enrich the IGM or re-accrete to enrich the infalling gas. This dynamic cycling of baryons in and out of galaxies shapes their stellar mass, metallicity, and star formation rate (SFR, e.g. M. S. Peeples & F. Shankar 2011; S. J. Lilly et al. 2013; P. Torrey et al. 2019). Galaxy metallicities are therefore one of the fundamental observational quantities that provide information about galaxy evolution, but they were largely unconstrained at $z > 3$ prior to the launch of *JWST* (but note e.g. T. Jones et al. 2020).

The measurement of the gas-phase metallicities of star-forming (SF) galaxies, traced by their oxygen abundance ($12 + \log(\mathrm{O/H})$), typically requires the detection of rest-frame optical emission lines that are absorbed by the Earth's atmosphere at $z \gtrsim 3$. *JWST*, with its unprecedented high-angular resolution and sensitivity in the near- and mid-infrared, has now begun to address this gap, offering routine detections of rest-frame optical emission lines at higher redshifts (e.g. K. Z. Arellano-Córdova et al. 2022; M. Curti et al. 2022; D. Schaerer et al. 2022; A. J. Taylor, A. J. Barger & L. L. Cowie 2022; J. R. Trump et al. 2023; J. Brinchmann 2023; A. C. Carnall et al. 2023; H. Katz et al. 2023b). This has enabled key metallicity scaling relations, such as the mass–metallicity relation (MZR) and fundamental metallicity relation (FMR), to be constrained out to $z \sim 10$ (e.g. K. E. Heintz et al. 2023a; K. Nakajima et al. 2023; M. Curti et al. 2024; I. Chemerynska et al. 2024; A. Sarkar et al. 2025; G. Venturi et al. 2024). However, the observational surveys used in these latest studies typically poorly sample the high-mass ($M_* > 10^9\,\mathrm{M}_\odot$) end of these relations, mainly due to limitations of survey volumes and due to the rarity of such massive systems at $z > 6$. Extending these metallicity studies to massive high-z galaxies is particularly important, as these galaxies likely represent both the descendants of the surprisingly bright galaxies discovered at $z > 10$ and the building blocks of the most massive structures observed at later times (e.g. T. Hashimoto et al. 2018; A. P. S. Hygate et al. 2023; D. Narayanan et al. 2025). Studying the metal content of massive $z > 6$ galaxies therefore provides a valuable foundation for exploring how early galaxies could have built up such high stellar and dust masses so soon after the big bang.

To address these challenges, a sample of spectroscopically confirmed massive galaxies in the Epoch of Reionization (EoR) is necessary. Amongst the largest contributions to this effort is the REBELS (Reionization Era Bright Emission Line Survey, R. J. Bouwens et al. 2022) ALMA large program, which has significantly expanded the sample of EoR galaxies with robust dust continuum and [C II] 158 μm detections. This survey targets 40 ultraviolet (UV)-bright ($M_{\mathrm{UV}} < -21.5$) galaxies at $z \sim 6.5$–9, resulting in a sample of 16 galaxies with confirmed dust continuum detections and 25 galaxies with [C II] detections (Schouws et al., in preparation; H. Inami et al. 2022). From this survey, 12 of the [C II]-brightest galaxies were targeted in *JWST* Cycle 1 programs (GO 1626: PI: M. Stefanon and GO 2659: PI: J. Weaver) with the *JWST* Near-Infrared Spectrograph integral field unit (NIRSpec/IFU). In this work, we present the emission-line fitting of these NIRSpec data, which we use to derive the oxygen abundances and other key ionized gas properties of these 12 galaxies.

This paper is structured as follows: in Section 2, we describe the data products from the REBELS program and the *JWST* NIRSpec observations. Section 3 details the methodology for extracting integrated spectra and fitting emission lines. In Section 4, we detail the derivation of the ionized gas properties of the sample, and in Section 5, we summarize the SED fitting used to derive the stellar population properties (with more details given in a subsequent paper, Stefanon et al., in preparation). We discuss the implications of our findings for the ionized gas properties of the REBELS galaxies, and put them into context by studying the MZR and FMR at $z \sim 6$–8 in Section 6. Finally, we summarize our work and conclusions in Section 7. Throughout this work, we assume a standard Lambda-cold dark matter cosmology (ΛCDM), with $H_0 = 70$ km s^{-1} Mpc^{-1}, $\Omega_m = 0.30$ and $\Omega_\Lambda = 0.70$. We further adopt a P. Kroupa (2001) initial mass function (IMF), and take solar abundance to be $12 + \log(\mathrm{O/H}) = 8.69$ (following M. Asplund et al. 2009).

2 DATA

The 12 galaxies analysed in this work were selected from the REBELS ALMA large program (R. J. Bouwens et al. 2022; Schouws et al., in preparation) and were observed with *JWST* NIRSpec/IFU in Cycle 1 (GO 1626, PI: M. Stefanon), with one source (REBELS-18) observed in GO 2659, PI: J. Weaver. All 12 of these galaxies have [C II] detections at $> 7\sigma$ from the REBELS large program, and all but two have continuum detections at rest-frame ~ 160 μm (H. Inami et al. 2022). We summarize key properties from the REBELS ALMA large program and pre-existing photometry in Table 1. The *JWST* observations of these sources were performed using the prism mode, covering an observed wavelength range of 0.6–5.3 μm with a spectral resolution of $R \sim 100$, for 1700 s of exposure per source (for REBELS-18, the exposure time is ~ 1.7 h). A full description of the reduction of the *JWST* data will be provided in Stefanon et al. (in preparation). Briefly, we employed a customized version of the *JWST* pipeline, incorporating the GRIZLI (G. Brammer 2023) implementation of Stage 1 with additional steps for cosmic ray masking using ASTROSCRAPPY (P. G. Dokkum 2001) and manual masking of hot edge pixels. For Stages 2 and 3, we used the default pipelines and parameters (albeit adopting 0.08 arcsec for the pixel scale). The final data cubes were background-subtracted by masking each main source and applying a 2D linear interpolation to reconstruct the background for each source.

2.1 Mask selection

In this work, we focus on the integrated spectrum and global properties of each galaxy. For the extraction of 1D spectra, we create source-specific apertures by combining masks that capture flux emission at $> 3\sigma$ in various wavelength ranges, including the rest-frame UV, rest-frame optical, and key emission lines such as [O II]λ3727, Hβ, [O III]λλ4959,5007, and Hα. These masks were merged to define the final aperture for each galaxy, covering all regions with significant flux detection. A full description of the masking procedure will appear in a forthcoming paper (Stefanon et al., in preparation). In Fig. 1, we show three colour-composite images of the 12 galaxies with the masks used to extract each spectrum in white, and in Fig. 2, we plot the integrated spectra

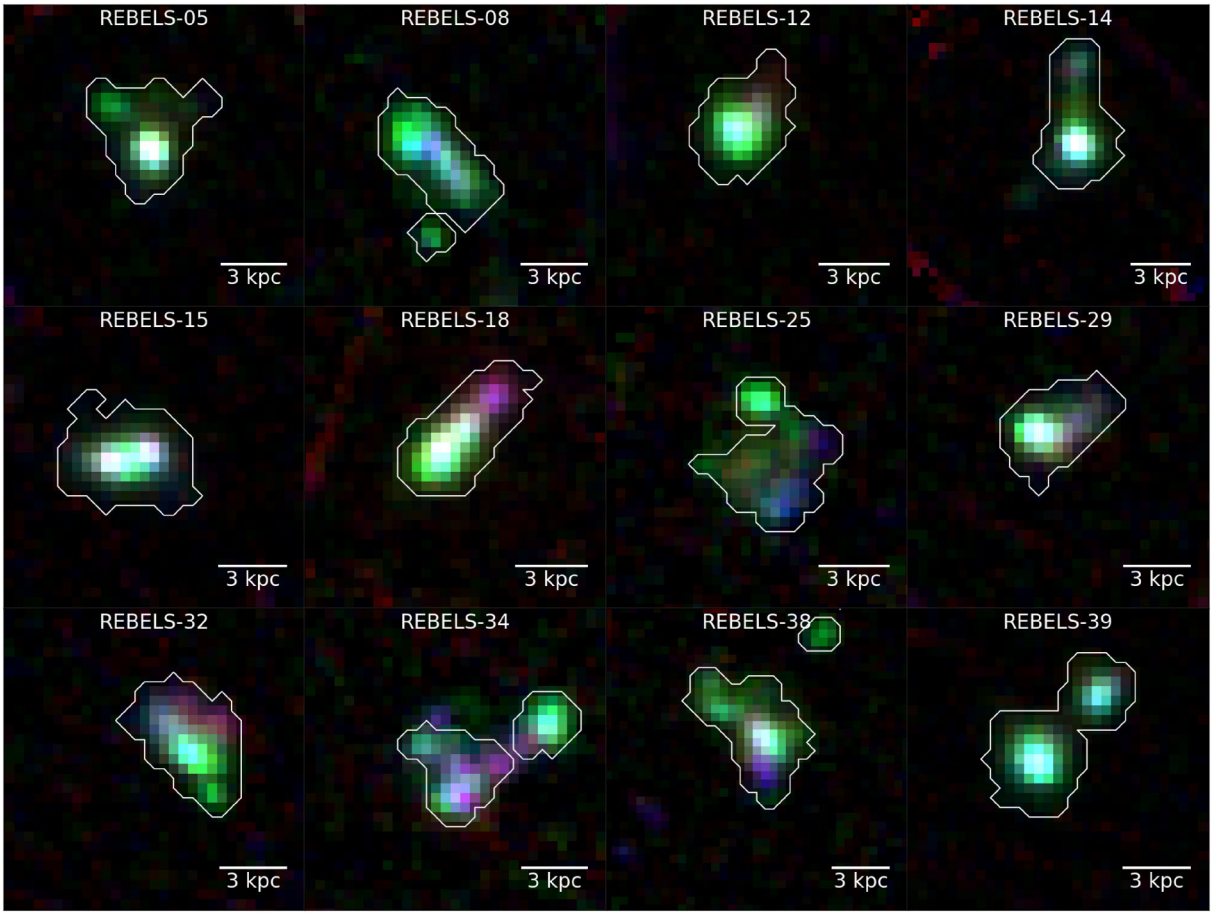

Figure 1. Three-colour composite images of each of the 12 REBELS galaxies targeted in the Cycle 1 *JWST* program analysed in this work. Red corresponds to rest-frame optical ($0.37 < \lambda_{\rm rest} < 0.855$ μm, excluding emission lines), green to [O III]λ5007, and blue to rest-frame UV emission ($0.12 < \lambda_{\rm rest} < 0.37$ μm, excluding emission lines). The white contours are used to extract the integrated spectrum of each galaxy, as described in the text.

extracted from these masks. In many cases, the emission is clumpy and irregular. For the purpose of this work, we derive properties based on the integrated spectrum of all the pixels contained within these masks, with further spatially resolved analyses to follow in subsequent works. We therefore caution that some sources, assumed in this work to be single objects, may in fact be merging or interacting systems.

3 EMISSION-LINE MEASUREMENTS

In order to model the observed emission lines, we first continuum-subtract the integrated spectra extracted from the masks. To do this, we fit a third-order polynomial to a portion of each spectrum (from $\lambda > 0.3$ μm in the rest-frame), excluding wavelengths where emission lines are detected, using the PYSPECKIT PYTHON package (A. Ginsburg et al. 2022). The continuum-line fits are show in Appendix A. We then fit all key nebular emission lines with $> 1\sigma$ emission at the expected wavelength centroid based on the redshift of each galaxy in the NIRSpec wavelength range using the Gaussian model within PYSPECKIT. To reduce the number of free parameters, we fix the centroid and width of each of the key emission lines according to the redshift and line spread function (LSF), since at the resolution of the prism grating the widths of the lines are dominated by the spectral resolution (see Appendix A). We also test subtracting the stellar continuum from the best-fitting spectral energy distribution (SED, discussed in Section 5), in order to account for stellar absorption at the hydrogen recombination lines, but note that this makes a negligible change to the derived emission-line fluxes, even for the Balmer lines, since we see very little stellar absorption. This suggests that the emission is dominated by bright, young stellar populations, which is perhaps not surprising considering these galaxies are UV-selected and amongst the most UV-bright in the EoR.

Due to the coarse resolution of the prism ($R \sim 100$), many of the key emission lines are blended. In addition, it is not possible to identify and fit broad components to the emission lines at the current spectral resolution. We therefore fit the following blended emission lines as single Gaussians: [OII]λ3727 + [OII]λ3729, [NeIII]λ3869 + HeI + Hζ, Hγ + [OIII]λ4363 + [FeII]λ4360, and [SII]λ6716 + [SII]λ6731. Note that we assume that the relative contribution of the fainter He I and Hζ lines is negligible, in comparison to the uncertainties, to the total flux around the [Ne III] emission line, and hereafter we assume that this blended feature is equivalent to only the [Ne III] flux. The Hα emission line is also blended with the [N II]λλ6548,84 doublet at the resolution of the prism. However, for the 8 sources at $z \lesssim 7$ where Hα is detected, the line is visibly asymmetric. We therefore fit a triple Gaussian to the blended lines in order to determine the Balmer decrement and obtain attenuation-corrected emission-line fluxes. To reduce the number of free parameters in this triple-Gaussian fit, as well as fixing the line widths and the line centres, we also tie the flux ratio

Table 1. Summary of the properties derived from pre-existing ground-based observations of our sample.

Galaxy	RA	Dec.	$z_{[CII]}$	$L_{[CII]}$ $10^8 L_\odot$	L_{IR} $10^{11} L_\odot$
REBELS-05	02:18:11.51	−05:00:59.3	6.496	$6.9^{+0.8}_{-0.9}$	$3.2^{+1.9}_{-1.2}$
REBELS-08	02:19:35.13	−05:23:19.2	6.749	$7.4^{+1.0}_{-1.1}$	$5.2^{+3.0}_{-2.0}$
REBELS-12	02:25:07.94	−05:06:40.7	7.349	10 ± 4	$2.8^{+29}_{-1.4}$ [b]
REBELS-14	02:26:46.19	−04:59:53.5	7.084	$3.7^{+1.1}_{-1.0}$	$3.3^{+2.0}_{-1.4}$
REBELS-15	02:27:13.11	−04:17:59.2	6.875	$1.9^{+0.5}_{-0.4}$	< 3.6
REBELS-18	09:57:47.90	02:20:43.7	7.675	$11^{+1.0}_{-0.9}$	$3.5^{+2.0}_{-1.3}$
REBELS-25	10:00:32.32	01:44:31.3	7.306	17 ± 2 [a]	$5.0^{+2.9}_{-1.0}$ [c]
REBELS-29	10:01:36.85	02:37:49.1	6.685	$5.5^{+1.0}_{-0.9}$	$2.9^{+1.7}_{-1.1}$
REBELS-32	10:01:59.07	01:53:27.5	6.729	$7.9^{+0.8}_{-0.9}$	$3.1^{+1.9}_{-1.3}$
REBELS-34	10:02:06.47	02:13:24.2	6.633	$6.9^{+2.6}_{-1.9}$	< 3.8
REBELS-38	10:02:54.05	02:42:12.0	6.577	$17^{+1.6}_{-1.5}$	$3.0^{+1.7}_{-0.6}$ [b]
REBELS-39	10:03:05.25	02:18:42.7	6.847	$7.9^{+2.5}_{-2.4}$	$4.2^{+2.4}_{-1.6}$

Notes: Right ascension (RA), declination (Dec.), and spectroscopic redshifts ($z_{[CII]}$) in columns 1, 2, and 3, respectively, are taken from R. J. Bouwens et al. (2022). Column 5 lists the [C II]158 μm luminosities from S. Schouws et al. (in preparation), and column 6 lists the IR luminosities taken from H. Inami et al. (2022) for detections in ALMA's band 6 assuming an emissivity index $\beta = 2.0$.[a] The [C II] luminosity for REBELS-25 is taken from A. P. S. Hygate et al. (2023). [b] The IR luminosities for REBELS-12 and REBELS-38, which have continuum detections/limits in two bands with ALMA, are taken from the fiducial case in H. S. B. Algera et al. (2024; $\beta = 2.0$, optically thin). [c] The IR luminosity of REBELS-25 is taken from from H. Algera et al. (2024).

of the [N II] doublet to 3.049 (P. J. Storey & C. J. Zeippen 2000), so that the only free parameters are the amplitudes of Hα and [N II]λ6584. For the sources where [N II]λ6584 is detected at $\gtrsim 3\sigma$, we find that this triple-Gaussian model produces a better fit than a single Gaussian by comparing the resulting Akaike Information Criterion and/or reduced chi-squared values, justifying our use of this method. Since this blended emission means that the [N II] and Hα fluxes are correlated, we propagate these correlated uncertainties when determining the ratio of [N II] to Hα in subsequent sections. An example of this triple-Gaussian fit is plotted in Fig. 3. We also fix the flux ratio of the [O III]$\lambda\lambda$4959,5007 doublet to the theoretical value of 2.98, but note the detected lines are consistent with this theoretical value within the uncertainties if not fixed, reinforcing the robustness of our data reduction.

We add that the fits are performed twice with PYSPECKIT, so that the residuals in each spectrum are used to estimate the uncertainties in the final fitted parameters (see A. Ginsburg et al. 2022). If the error spectrum from the 'ERR' extension of the data cube is instead used, the uncertainties typically decrease by a factor of three. We use the larger uncertainties in the integrated fluxes to be conservative. A similar discrepancy with the reported flux uncertainties in the 'ERR' extension is also noted in H. Übler et al. (2023).

3.1 Reddening correction

The NIRSpec prism observations for eight of our targets provide us with coverage of both the Hα and Hβ lines, allowing us to estimate reddening corrections on the basis of the Balmer decrement. For each source, the nebular colour excess, $E(B-V)_{neb}$, is calculated from the Balmer decrement of each galaxy assuming Case B recombination at $T \sim 10^4$ K and electron density $n_e \sim 100$ cm^{-3} with an intrinsic ratio of 2.86 for Hα/Hβ (typical for H II regions, D. G. Hummer & P. J. Storey 1987; D. E. Osterbrock & G. J. Ferland 2006). This ratio is weakly sensitive to density and temperature (e.g. varying from 2.86 to 2.81 for $n_e = 10^2 - 10^6$ cm^{-3} at $T = 10^4$ K, with detailed values in, for example, M. A. Dopita & R. S. Sutherland 2003; D. E. Osterbrock & G. J. Ferland 2006). These small variations are negligible compared to dust effects, making the Balmer decrement a reliable diagnostic of reddening. We then make use of the measured Balmer decrements and the D. Calzetti et al. (2000) attenuation curve to correct the observed fluxes of various emission lines.

The continuum-subtracted, attenuation-corrected fluxes for these eight sources, which are listed in Table 2, are then used for all following calculations with the uncertainties returned by PYSPECKIT propagated through. We also determine the nebular visual attenuation, $A_{V,neb}$, for each galaxy from the product of the colour excess and the total-to-selective attenuation, for which we adopt the value of 4.1±0.8 derived by D. Calzetti et al. (2000). We note that the results presented in this paper do not significantly change if we had instead adopted a Milky Way attenuation curve (J. A. Cardelli, G. C. Clayton & J. S. Mathis 1989) or Large Magellanic Cloud attenuation curve (E. L. Fitzpatrick 1999), and a more detailed analysis of the dust attenuation within these galaxies will be the focus of a subsequent paper (R. Fisher et al. in preparation). The main findings of this paper are also consistent when the attenuation curve empirically derived from the NIRSpec data for each source (R. Fisher et al. 2025) is used.

For the four galaxies where Hα is beyond the wavelength coverage of NIRSpec, we do not attempt a reddening correction of the emission-line fluxes based on the Hγ/Hβ ratio, since these lines are detected at lower signal-to-noise ratios (SNRs) than Hα, increasing the uncertainty in the derived $A_{V,neb}$, and because the observed Hγ/Hβ ratios are consistent with unphysical values (assuming Case B recombination) for the majority of the sample, likely as a consequence of the low SNR detections. More details are given in Appendix B. We therefore give the non-attenuation-corrected values for these four $z \gtrsim 7$ galaxies in Table 3, and for all subsequently derived quantities that depend strongly on dust (e.g. O32, $\log U$, and SFR) we report limits instead. In addition, we have tested the impact of applying dust corrections based on the stellar dust attenuation ($A_{V,*}$) derived from the SED fitting (presented in Stefanon et al. in preparation; R. Fisher et al. 2025). We explore two scenarios: assuming equal stellar and nebular attenuation, and adopting a scaling between the two ($A_{V,*} = 0.44 A_{V,neb}$, following D. Calzetti, A. L. Kinney & T. Storchi-Bergmann 1994). We find that the resulting change in the derived properties is always within the quoted uncertainties.

4 IONIZED GAS PROPERTIES

With the detected emission lines, we derive the oxygen abundance ($12 + \log(O/H)$), ionization parameter ($\log U$), and SFR of each galaxy. For these calculations, we adopt the following standard definitions for line ratios:

$$R3 = [OIII]\lambda 5007/H\beta \quad (1)$$

$$N2 = [NII]\lambda 6584/H\alpha \quad (2)$$

$$S2 = [SII]\lambda\lambda 6716, 31/H\alpha \quad (3)$$

$$R23 = \frac{[OIII]\lambda\lambda 4959, 5007 + [OII]\lambda\lambda 3727, 29}{H\beta} \quad (4)$$

$$O32 = [OIII]\lambda 5007/[OII]\lambda\lambda 3727, 29 \quad (5)$$

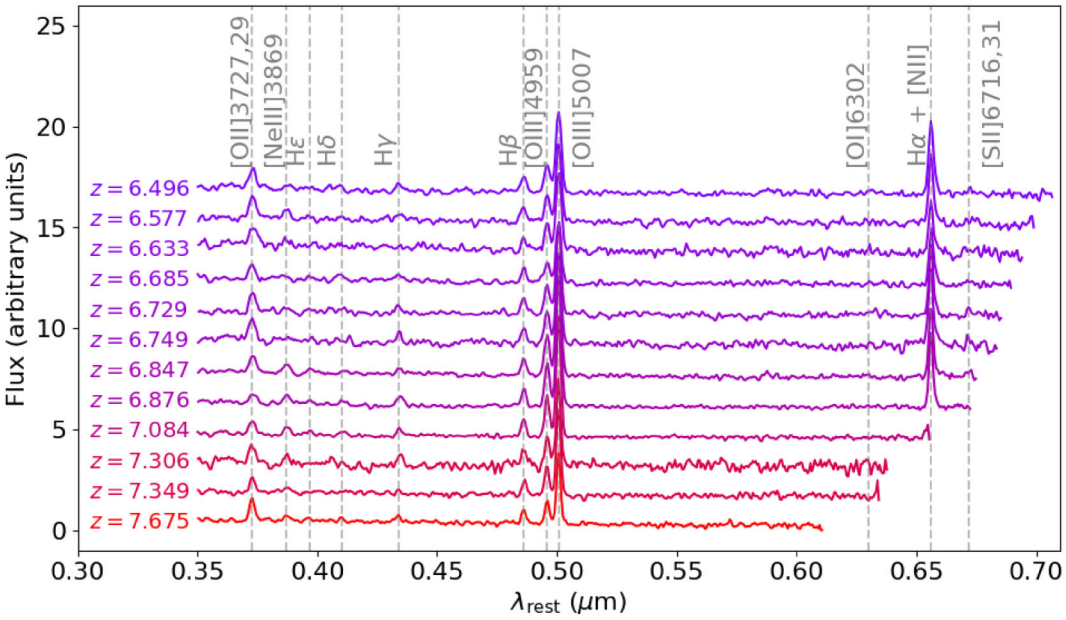

Figure 2. Integrated NIRSpec spectrum of all 12 REBELS targeted with our IFU program, extracted from a target-specific aperture mask shown in Fig. 1. Each spectrum is only shown over the range $\lambda_{\rm rest} = 0.35$ μm to $\lambda_{\rm obs} = 5.3$ μm to highlight the key detected rest-frame optical emission lines, labelled with the grey dashed lines and text. The fluxes are normalized to the Hβ flux of each galaxy, and offset along the vertical axis for clarity. The redshift of each REBELS galaxy is indicated by labels on the left-hand side, ordered from top to bottom in increasing redshift.

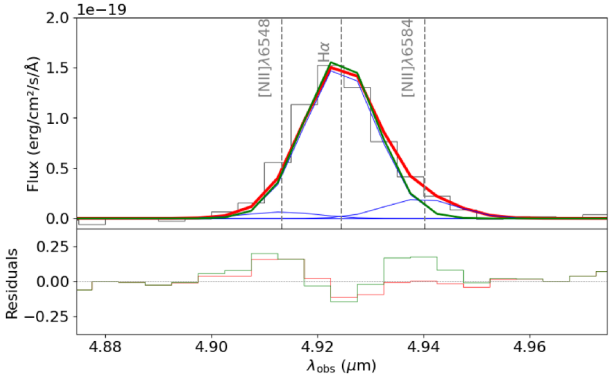

Figure 3. An example of the triple-Gaussian fit to the [N II]λ6548, Hα, and [N II]λ6584 blended spectral feature for REBELS-05 is shown in red, with each component plotted in blue, in the top panel. We also show a single-Gaussian fit to Hα only in green. In the bottom panel, we plot the residuals of the triple-Gaussian fit (red) and the single-Gaussian fit (green).

$$\mathrm{Ne3O2} = [\mathrm{NeIII}]\lambda3869/[\mathrm{OII}]\lambda\lambda3727,29 \quad (6)$$

$$\mathrm{O2} = [\mathrm{OII}]\lambda\lambda3727,29/\mathrm{H}\beta \quad (7)$$

For these line ratios, [OII]λλ3727, 29, [OIII]λλ4959, 5007, and [SII]λλ6716, 31 denotes the sum of the corresponding doublets.

4.1 Ionization state

Before deriving the ISM properties of these galaxies, we first investigate their source of ionization, in particular to examine potential contamination from active galactic nuclei (AGNs). Emission-line diagnostic diagrams, such as BPT (J. A. Baldwin, M. M. Phillips & R. Terlevich 1981), VO87 (S. Veilleux & D. E. Osterbrock 1987), and 'OHNO' or ionization-metallicity (B. E. Backhaus et al. 2022) diagrams are often used to investigate the ionization state of galaxies and regions of ionized gas. For example, in the local Universe, gas predominantly ionized by star formation typically follows well-defined sequences in these diagrams (e.g. L. J. Kewley et al. 2001; G. Kauffmann et al. 2003), whereas gas ionized by harder ionizing sources, like AGNs, typically shows enhanced N2 and S2 ratios. We plot the BPT and VO87 diagnostic diagrams in Fig. 4 for the 12 REBELS galaxies, as well as galaxies in the literature at $z \sim 0$ from the SDSS (Sloan Digital Sky Survey) data release 8 catalogue, $z \sim 2-3$ from MOSFIRE Deep Evolution Field (MOSDEF; A. E. Shapley et al. 2015), and sources from *JWST* Advanced Deep Extragalactic Survey (JADES) data release 3 catalogues (F. D'Eugenio et al. 2025).

For nearby galaxies, the empirical demarcation lines from L. J. Kewley et al. (2001) and G. Kauffmann et al. (2003) are typically used to distinguish between AGN, SF, and composite galaxies in the BPT and VO87 diagrams. However, at high redshifts, these demarcations may no longer be applicable since studies have shown that galaxies at high redshift do not lie on the same loci of nebular line ratios as local galaxies (e.g. A. E. Shapley et al. 2005; X. Liu et al. 2008; C. C. Steidel et al. 2014; A. L. Strom et al. 2017). This offset from the local sequence at high-z is likely driven by a difference in ionization properties, such as lower metallicities and harder ionizing fields. For this reason, a recent study (J. Scholtz et al. 2025) has defined new, conservative demarcation lines for the BPT and VO87 diagrams based on SF models from J. Gutkin, S. Charlot & G. Bruzual (2016). However, [N II] and [S II] are largely undetected at $z > 4$, even in large-scale surveys like JADES and CEERS (Cosmic Evolution Early Release Science), meaning statistics are limited in testing these demarcations. In a sample of 38 galaxies at $5 \leq z < 6.5$ from the CEERS survey studied in R. L. Sanders et al. (2023), there is only one detection of [S II], and six detections of [N II]. From the JADES survey, as analysed in A. J. Cameron et al. (2023), there are only three detections (in a sample of 20 galaxies at $5.5 < z < 6.9$) of [S II] and

Table 2. Attenuation-corrected emission-line fluxes for the eight galaxies where Hα lies within the NIRSpec wavelength coverage. Fluxes are quoted in units of 10^{-18} erg s^{-1} cm^{-2} with their uncertainties. Where the SNR<3, we report the 3σ upper limits on the flux. Dashes represent emission lines that are redshifted out of the NIRSpec wavelength range.

Galaxy	[O II]^a	[Ne III]3869^b	Hϵ	Hδ	Hγ^c	Hβ	[O III]5007	[O I]6302	Hα^d	[N II]6584^d	[S II]^e
REBELS-05	38 ± 4	<8.8	<6.7	<14	9.2 ± 2.5	19 ± 2	93 ± 2	<4.4	53 ± 2	6.8 ± 1.6	<5.4
REBELS-08	44 ± 5	<13	<11	<8.2	13 ± 3	18 ± 3	100 ± 2	<4.8	51 ± 2	8.3 ± 1.6	5.3 ± 1.6
REBELS-15	19 ± 4	16 ± 3	<6.2	<7.5	16 ± 3	24 ± 2	180 ± 2	<2	69 ± 2	<9.4	-
REBELS-29	11 ± 1	<3.2	<3.2	3.8 ± 1.0	5.4 ± 1.5	8.1 ± 0.9	35 ± 1	<1.9	23 ± 1	3.3 ± 0.7	<2.5
REBELS-32	23 ± 2	<5.9	<4.4	<5.4	6.5 ± 1.5	13 ± 1	71 ± 1	<1.9	37 ± 1	3 ± 1	3.2 ± 0.9
REBELS-34	29 ± 4	<9.3	<8.2	<5.5	<4.6	8.8 ± 1.8	64 ± 2	<5.6	25 ± 1	<5.6	<17
REBELS-38	59 ± 5	23 ± 4	<8.8	<8.2	14 ± 5	21 ± 3	110 ± 31	<6.4	60 ± 2	6.2 ± 1.9	<15
REBELS-39	29 ± 4	13 ± 3	<7	<6.1	<9.6	20 ± 2	150 ± 2	<3	57 ± 2	<6.6	<4.2

Notes. [a] Blended [O II]$\lambda\lambda$3727,9 doublet, [b] blended with He I and Hζ, however for the purpose of this work we assume that the contribution from these fainter lines is negligible in comparison to the uncertainties. [c] Blended with the auroral [O III]λ4363 line and the [Fe II]λ4360 line, however for the purpose of this work we assume that the contribution from these fainter lines is negligible in comparison to the uncertainties. [d] The Hα and [N II]$\lambda\lambda$6548,84 doublet are blended in the prism mode. However, owing to the larger SNR and the increased resolution at the red end of the spectrum, we are able to fit a triple Gaussian to this spectral feature, as described in the text and shown in Fig. 3. The ratio of [N II]λ6584/[N II]λ6548 is fixed to the theoretical value of 3.049. [e] Blended [S II]$\lambda\lambda$6716,31 doublet.

Table 3. We present the emission-line fluxes without attenuation-correction for the four REBELS galaxies where Hα is beyond the wavelength range of NIRSpec, with the same format as in Table 2.

Galaxy	[O II]	[Ne III]3869	Hϵ	Hδ	Hγ	Hβ	[O III]5007	[O I]6302
REBELS-12	7.1 ± 0.6	2.9 ± 0.9	<1.9	<1.4	<2.9	6.1 ± 0.6	38 ± 1	–
REBELS-14	11 ± 1	5.8 ± 0.7	2.6 ± 0.7	2.3 ± 0.7	4.6 ± 0.7	11 ± 1	78 ± 1	–
REBELS-18	7.9 ± 0.4	1.9 ± 0.5	<1.2	<1.9	2.2 ± 0.5	4.3 ± 0.4	21 ± 0.4	–
REBELS-25	6.2 ± 0.7	2.5 ± 0.6	<14	<0.19	3.1 ± 0.6	5.2 ± 0.7	21 ± 1	<1.3

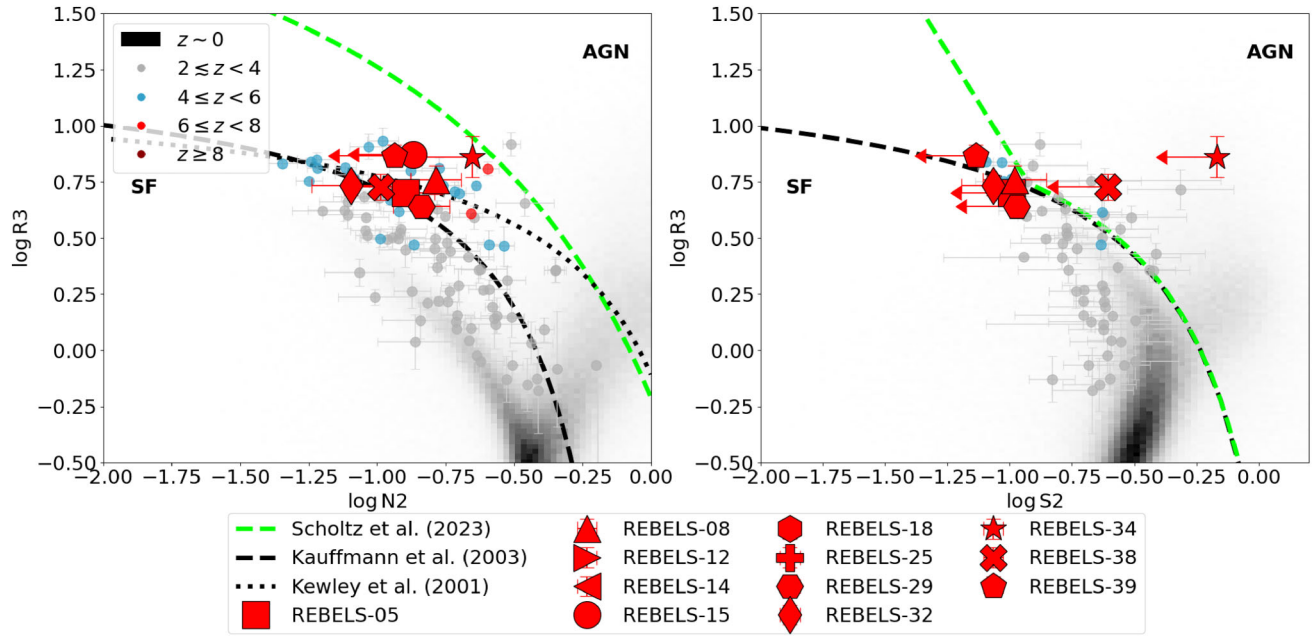

Figure 4. We plot the BPT diagram of R3 against N2 (left panel) and the VO87 diagram of R3 against S2 (right panel) for the the REBELS galaxies where Hα is within the NIRSpec wavelength coverage (red markers) and other high-z galaxies from the literature (coloured by redshift, as indicted in the legend in the left panel, taken from JADES data release 3; F. D'Eugenio et al. 2025, and MOSFIRE; A. E. Shapley et al. 2015). In comparison to empirical and theoretical demarcation lines used to distinguish between SF galaxies and those with AGNs (L. J. Kewley et al. 2001; G. Kauffmann et al. 2003; J. Scholtz et al. 2025), we find that the REBELS sources are mostly consistent with ionization predominantly by star formation.

no detections of [N II] (in a sample of 18 galaxies at $5.5<z<6.9$), with [N II] also undetected in a stack of all 18 spectra. In contrast, with just 30 min of exposure per source of the REBELS galaxies, [N II]λ6584 is detected at $>3\sigma$ for five out of eight galaxies with the correct wavelength coverage in the REBELS-IFU sample (tentatively detected at $\gtrsim2\sigma$ for the remaining three), and [S II] is detected

at $> 3\sigma$ in two out of seven (tentatively detected at $\gtrsim 2\sigma$ for an additional three sources). However, we again emphasize the caveat that the [N II] line is blended with Hα, increasing the uncertainty of the N2 ratio derived from the prism spectra.

From these BPT and VO87 diagnostic plots, we see no strong evidence of AGN activity within the REBELS sources, since all detections lie below the conservative J. Scholtz et al. (2025) demarcation line. For REBELS-34 and REBELS-38, whilst their 3σ upper limits on S2 lie above this demarcation in the VO87 diagram, they lie below it on the BPT diagram. There are, however, some potential AGN candidates (REBELS-15, REBELS-34, and REBELS-39) that show slightly elevated R3 ratios in comparison to the L. J. Kewley et al. (2001) and G. Kauffmann et al. (2003) demarcations within the sample. However, these sources, and the use of these diagnostics to identify AGN at high-z, would require further study to confirm or deny the presence of AGN. Follow-up *JWST* Cycle 3 observations (GO-6480, PI: S. Schouws) of galaxies from the REBELS sample may shed further light on the nature of these sources by obtaining high spatial resolution imaging with grism spectroscopy, which will enable, for example, a search for broad emission-line features which are also characteristic of AGN activity.

In Fig. 5, we plot two different ionization-metallicity diagnostic diagrams – R3 versus Ne3O2, and R23 versus O32 – for the REBELS galaxies and the aforementioned literature samples spanning $z = 0$ to $\gtrsim 8$, with the addition of $z > 4$ sources from the PRImordial gas Mass AssembLy survey (PRIMAL; K. E. Heintz et al. 2025), which includes sources from CEERS (ERS-1345; S. L. Finkelstein et al. 2023), GLASS-DDT (DDT-2756 T. Treu et al. 2022), JADES (GTO-1180, 1210, GO-3215; A. J. Bunker et al. 2023; D. J. Eisenstein et al. 2023), and UNCOVER (GO-2561; R. Bezanson et al. 2024). Whilst we find similar R3 and R23 ratios to other $z \gtrsim 6$ galaxies, the REBELS sources show lower O32 and Ne3O2 ratios (and also O2 ratios). Recent *JWST* observations find O32 ratios typically between 7 to 31, Ne3O2 $\sim$ 1–2 and O2 $\gtrsim 5$ from reionization-era galaxies (S. Mascia et al. 2023; J. E. Rhoads et al. 2023; R. L. Sanders et al. 2023; M. Tang et al. 2023; G. Roberts-Borsani et al. 2024). In low-redshift galaxies, such high O32, Ne3O2, and O2 ratios are mostly associated with extreme [O III] emitters (M. Tang et al. 2019) and/or those with high ionization parameter and low metallicity (A. L. Strom et al. 2018; C. Papovich et al. 2022). In contrast, all but two of the REBELS galaxies have O32 ratios < 5, with Ne3O2 and O2 ratios $\lesssim 0.8$ across the entire sample. This suggests that the REBELS galaxies probe different ISM conditions compared to other existing spectroscopic surveys at $z > 6$, likely representing more evolved, metal-rich galaxies with less extreme ionizing conditions. In addition, existing large *JWST* surveys may be more biased toward galaxies with high O32 values and high [O III] EWs. In contrast, the [O III] EWs of our sample (listed in Table 4) are more consistent with the median [O III] EW at $z \sim 7$ of ~ 450 Å (I. Labbé et al. 2013), suggesting that the REBELS galaxies may provide a more representative view of the general galaxy population at these redshifts, rather than being skewed toward extreme-line emitters.

Assuming these sources are predominantly ionized by star formation, we compare with photoionization models from `HII-CHI-Mistry` (E. Pérez-Montero 2014). These models used the synthesis spectral code CLOUDY v13.03 (G. J. Ferland et al. 2013) using `POPSTAR` (M. Mollá, M. L. García-Vargas & A. Bressan 2009) stellar evolutionary models assuming an instantaneous burst with an age of 1 Myr with an IMF from G. Chabrier (2003). They varied the ionization parameter between $-4.00 \leq \log(U) \leq -1.50$ in steps of 0.25 dex, the oxygen abundance between $7.1 \leq 12 + \log(\mathrm{O/H}) \leq 9.1$ in steps of 0.1 dex, and considered variations in the N/O ratio between $0.0 \leq \log(\mathrm{N/O}) \leq -2.0$ in steps of 0.125 dex, thus totalling 3927 models. We plot grids of these models for N/O values of -1.0 and 0.0 in the bottom panels of Figs 4 and 5. Here, we see that the REBELS galaxies lie in a parameter space with ionization parameters $\log U \lesssim -2$, but with multiple solutions for the oxygen abundance.

To assess the ISM properties of these sources, we first further investigate their ionization parameters. The ionization parameter, $\log U$, is commonly defined as the ratio of ionizing photon density to hydrogen density and can be used to indicate the ionization state (e.g. C. B. Tarter, W. H. Tucker & E. E. Salpeter 1969). It is often derived from the O32 ratio, as this ratio represents the relative abundance between doubly ionized oxygen to singly ionized oxygen (A. L. Strom et al. 2018; L. J. Kewley et al. 2019; C. Papovich et al. 2022). To estimate $\log U$ from O32, we use the calibrations empirically derived in C. Papovich et al. (2022) from a sample of galaxies at $z \sim 1.1 - 2.3$. We list these derived values in Table 4. We find a range of $\log U$ from -2.5 to -1.9, and we find that these values are consistent within the uncertainties when derived using the calibrations from A. I. Díaz et al. (2000) and L. J. Kewley et al. (2019), and when using the aforementioned `HII-CHI-Mistry` code. However, we note that these calibrations are based on lower redshift sources, and may therefore need some adjustment at $z > 6$.

Having found that these galaxies exhibit lower O32 ratios, and therefore lower ionization parameters, than many other high-z sources in the literature, we may therefore expect to find higher metallicities in comparison to the literature samples (e.g. R. L. Sanders et al. 2021). We describe the methods used to derive the metallicities of these galaxies below.

4.2 Gas-phase metallicity

A variety of both empirical and theoretical strong-line metallicity calibrations exist within the literature. Prior to the launch of *JWST*, empirical calibrations were based on high-z analogues in the local Universe (e.g. R. Maiolino et al. 2008; M. Curti et al. 2020; F. Bian, L. J. Kewley & M. A. Dopita 2018; K. Nakajima et al. 2022). However, the use of calibrations based on local analogs may be unreliable for high-z galaxies due to evolving ISM conditions, which can alter the relationship between strong-line ratios and gas-phase metallicity, potentially skewing the derived oxygen abundances. More recently, thanks to the growing number of auroral line detections at $z > 2$, new high-z calibrations have now been derived and tested (R. L. Sanders et al. 2024). The strong-line calibrations derived in R. L. Sanders et al. (2024), based on 46 auroral line detections at $1.4 \leq z \leq 8.7$, are calibrated for $7.0 \leq 12 + \log(\mathrm{O/H}) \leq 8.4$. However recent auroral line detections at $z \sim 2 - 3$ up to $12 + \log(\mathrm{O/H}) \sim 8.5$ from the MARTA (Measuring Abundances at high Redshift with the T_e Approach) survey find good agreement with these calibrations (E. Cataldi et al. 2025) as do absorption-line-based gas-phase metallicities at $z \sim 2 - 4$ up to $12 + \log(\mathrm{O/H}) \sim 8.7$ (P. Schady et al. 2024).[1] We therefore adopt these calibrations to derive the fiducial metallicities for our sample. We also provide a comparison with other calibrations (F. Bian et al. 2018; K. Nakajima et al. 2022; I.

[1] In table D1 of P. Schady et al. (2024), the low-branch solutions using the R3 and R23 (R. L. Sanders et al. 2024) calibrations are listed. However, based on the emission-line fluxes reported therein, we re-derive the metallicities, using the O32 ratio to choose between the low-branch and extrapolated high-branch solutions, and find better agreement with the absorption line-based metallicities, increasing our confidence in extrapolating the R. L. Sanders et al. (2024) calibrations to higher oxygen abundances.

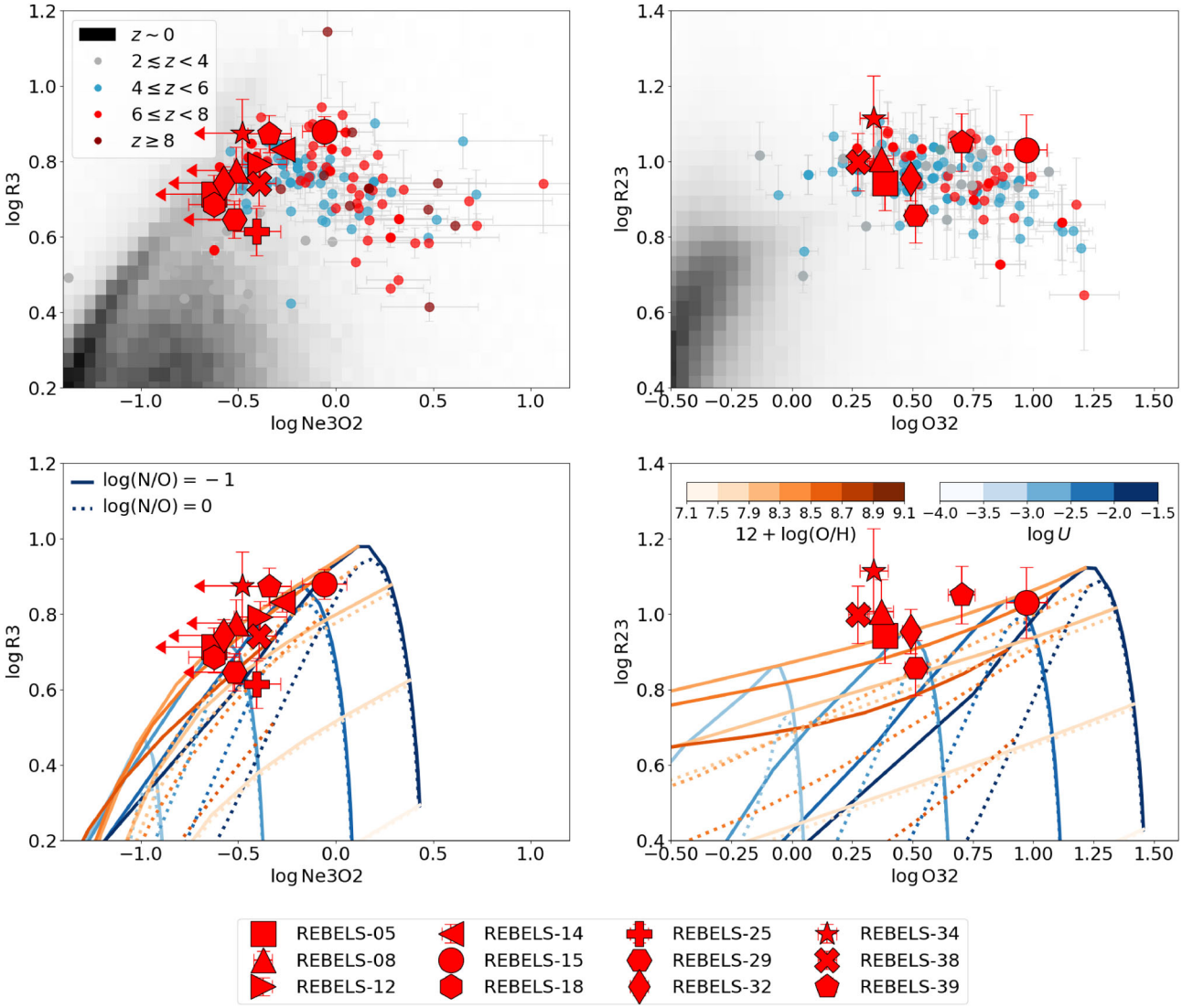

Figure 5. We present two emission-line ratio diagrams that can be used to trace the ionization and metallicity of galaxies. In the left panels, we show R3 versus Ne3O2 using emission-line ratios without attenuation correction for all 12 of the REBELS galaxies analysed in this work, as these lines are close in wavelength. For five of the REBELS galaxies, the [Ne III] line is detected at $< 3\sigma$, and we therefore show these Ne3O2 ratios as 3σ upper limits. In the right panels, we plot R23 versus O32 for only the eight REBELS galaxies where attenuation-corrected fluxes have been derived (see the text). In the top panels, we compare the REBELS galaxies to literature samples across various redshifts, including SDSS galaxies at $z \sim 0$, MOSDEF (A. E. Shapley et al. 2015) galaxies at $z \sim 2-4$, and sources from the PRIMAL survey (K. E. Heintz et al. 2025, full references given therein) for $z > 4$. In the bottom panels, we compare the position of the REBELS galaxies on these diagrams with CLOUDY photoionization model grids at different values of $12 + \log(\mathrm{O/H})$, $\log U$, and $\log(\mathrm{N/O})$. We find that most of the REBELS galaxies have O32 and Ne3O2 ratios towards the lower end of those $z > 6$ galaxies in existing surveys, indicating lower ionization parameters and higher metallicities.

H. Laseter et al. 2024) and with the `genesis-metallicity` calibrator (D. Langeroodi & J. Hjorth 2024) in Appendix C, and we detail the caveats in Section 4.2.1, below.

Of the different strong-line ratios found to correlate with metallicity, the R23 index is generally found to show the least scatter, and is used often in the literature in both the nearby Universe (e.g. see C. A. Tremonti et al. 2004, and references therein) and now out to high redshifts (e.g. K. Nakajima et al. 2023). We therefore use this ratio where possible. However, for the four galaxies where Hα is not detected and a reddening-correction is not applied, we instead use the R3 ratio, which is less impacted by interstellar reddening and flux calibration uncertainties. A limitation of using the R23 and R3 ratios as metallicity callibrators is that they typically yield two different metallicity estimates for the same ratio. Following, for example, M. Curti et al. (2024); L. J. Kewley & S. L. Ellison (2008); K. Nakajima et al. (2023); and A. Sarkar et al. (2025), we use the O32 and Ne3O2 ratio or upper limit to select the branch of the R23 and R3 relations. As indicated from the lower O32 ratios discussed in Section 4.1, the high branch solution is preferred for all but one of the REBELS galaxies. For the remaining galaxy, REBELS-14, both solutions are consistent with the peak of the R3 relation at $12 + \log(\mathrm{O/H}) \sim 7.92$, and we therefore take the two solutions as upper and lower bounds for its oxygen abundance, as in K. Nakajima et al. (2023).

We note that for three galaxies (REBELS-15, REBELS-34, and REBELS-39), there is no solution for the R3 or R23 calibration due

Table 4. Summary of the properties derived from the NIRSpec/IFU data analysed in this work. Columns show the nebular attenuation (A_V), [O III]λ5007 EW, O32 ratio, ionization parameter (log U), oxygen abundance ($12 + \log(O/H)$), stellar mass ($\log(M_*/M_\odot)$, Stefanon et al., in preparation) and star formation rates from the observed Hβ luminosity ($SFR_{H\beta}$). For the four sources at $z \gtrsim 7$, the O32 ratios given are upper limits since no attenuation-correction is applied.

Galaxy	$A_{V,\ neb}$ (mag)	$EW_{[OIII]5007}$ (Å)	O32	log U	$12 + \log(O/H)$	log $M_*/M_\odot$	$SFR_{H\beta}$ ($M_\odot$ yr^{-1})
REBELS-05	0.95 ± 0.42	459 ± 27	2.43 ± 0.31	-2.37 ± 0.04	8.51 ± 0.16	$9.42^{+0.10}_{-0.10}$	137 ± 16
REBELS-08	1.21 ± 0.51	510 ± 40	2.35 ± 0.30	-2.39 ± 0.04	8.22 ± 0.20	$9.33^{+0.07}_{-0.06}$	143 ± 21
REBELS-12	–	435 ± 20	< 5.31	< -2.08	8.23 ± 0.20	$9.54^{+0.03}_{-0.04}$	> 26
REBELS-14	–	1046 ± 58	< 7.16	< -1.97	7.90 ± 0.12 [a]	$9.24^{+0.07}_{-0.06}$	> 45
REBELS-15	0.67 ± 0.32	1259 ± 87	9.38 ± 1.20	-1.87 ± 0.07	7.78 ± 0.30	$9.31^{+0.02}_{-0.01}$	204 ± 18
REBELS-18	–	234 ± 8	< 2.67	< -2.34	8.50 ± 0.13	$9.71^{+0.06}_{-0.04}$	> 21
REBELS-25	–	511 ± 56	< 3.42	< -2.25	8.62 ± 0.17	$9.30^{+0.12}_{-0.14}$	> 22
REBELS-29	0.34 ± 0.40	296 ± 14	3.26 ± 0.42	-2.27 ± 0.04	8.73 ± 0.15	$9.69^{+0.07}_{-0.05}$	64 ± 7
REBELS-32	0.68 ± 0.35	559 ± 33	3.10 ± 0.40	-2.28 ± 0.03	8.48 ± 0.13	$9.57^{+0.10}_{-0.08}$	104 ± 10
REBELS-34	1.06 ± 0.74	283 ± 13	2.18 ± 0.28	-2.41 ± 0.05	8.33 ± 0.29	$9.45^{+0.03}_{-0.02}$	68 ± 14
REBELS-38	1.14 ± 0.47	347 ± 17	1.88 ± 0.24	-2.47 ± 0.03	8.28 ± 0.18	$9.75^{+0.09}_{-0.06}$	159 ± 21
REBELS-39	0.62 ± 0.40	1030 ± 58	5.05 ± 0.64	-2.10 ± 0.05	8.02 ± 0.29	$9.35^{+0.09}_{-0.08}$	167 ± 19

Notes. [a] For REBELS-14, the upper and lower branch solutions to the R3 calibration are consistent within the uncertainties with the calibration peak. Therefore, we adopt the average of these solutions as the oxygen abundance and the range between them as the uncertainty.

to their high R3 and R23 ratios. For these galaxies, we use the O32 ratio to estimate the oxygen abundance.

Although this study focuses on the integrated properties of each galaxy, the NIRSpec/IFU data also reveal spatial structure in several sources, with some appearing to host multiple clumps or components. To test whether these components exhibit significantly different metallicities compared to the integrated values, we performed a basic clump-by-clump analysis using the [O III]λ5007 emission maps. We used the ASTRODENDRO[2] PYTHON package to identify spatially distinct clumps and extracted 1D spectra for those with sufficient SNR. For the galaxies REBELS-05, -08, -34, -38, and -39, we successfully measured the metallicity of multiple clumps using the same strong-line methodology as for the integrated spectra. Comparing the clump-based metallicities with the integrated values, we find that for the O32 calibration, the differences range from –0.19 to +0.25 dex, with an average offset of just –0.003 dex. For the R3 calibration, the differences span from –0.10 to +0.34 dex, with an average offset of + 0.07 dex. These modest variations indicate that, while localized abundance variations exist, the integrated metallicities remain broadly representative of the systems as a whole. A more detailed analysis of the spatially resolved metallicities will be presented in a forthcoming paper.

The oxygen abundances for the sample are listed in Table 4. Notably, all galaxies are found to have $Z_g > 0.1 Z_\odot$, and we find some near-solar and potentially even super-solar oxygen abundances within the sample. However, it is important to treat these absolute values with caution due to the significant systematic uncertainties associated with strong-line calibrations. For consistency, we focus on comparing our results with other high-z galaxies in the literature where we have applied the same calibration methodology. We discuss the various caveats in our derived oxygen abundances in more detail below.

[2] http://www.dendrograms.org/

4.2.1 *Caveats*

Even in the local Universe, where metallicity calibrations are widely studied, metallicities estimated through different strong-line ratios and calibrations can vary by as much as ~ 0.6 dex (L. J. Kewley & S. L. Ellison 2008; J. Moustakas et al. 2010; L. E. Rowland et al. 2024b). At high-z, where the number of auroral line detections is lower and ionizing conditions are less well understood, discrepancies are likely to be even greater. The R. L. Sanders et al. (2024) calibrations adopted in this paper are based on a sample size of only 46 galaxies, over half of which are at $z < 5$. It is clear that a more significant sample of auroral line detections at high-z is essential for improving these calibrations, although we note that auroral line detections reported since the publication of R. L. Sanders et al. (2024) have found good agreement with these calibrations (e.g. I. H. Laseter et al. 2024), even out to $z = 10.17$ (T. Y.-Y. Hsiao et al. 2025).

The main source of uncertainty with our use of these calibrations is that they are only calibrated up to $12 + \log(O/H) \sim 8.4$, meaning that for five galaxies in our sample, we are extrapolating. The same issue is present in, for example, the F. Bian et al. (2018) and K. Nakajima et al. (2022) calibrations. The general expectation has been that high-z galaxies would be metal-poor, meaning that most calibrations based on local analogs have focused on extremely meal-poor galaxies. Recent findings of a mature, metal-rich galaxy at $z = 6.7$ (A. E. Shapley et al. 2025), as well as the REBELS galaxies studied here, highlight that it is now necessary to extend these calibrations to higher metallicities.

Additionally, there are also caveats to consider in the choice of line ratio used to derive the oxygen abundance. Whilst the R23 and R3 ratios are found to be the most accurate metallicity indicators at high-z (K. Nakajima et al. 2023; I. H. Laseter et al. 2024), they span only a narrow dynamic range at these redshifts (~ 0.4 dex in Figs 4 and 5; see also R. L. Sanders et al. 2021), mostly scattered around the turnover regime between the 'upper' and 'lower' branches of these indices. It could therefore be argued that more linear calibrations, such as O2, O32, and Ne3O2, may provide more reliable extrapolations. However, they have a greater intrinsic scatter in R. L. Sanders et al. (2024) and recent studies have found

that these ratios may not be good indicators of metallicity at these redshifts (e.g. I. H. Laseter et al. 2024). They are also generally not recommended at lower redshifts due to their strong, primary dependence on the ionization parameter (e.g. L. J. Kewley & M. A. Dopita 2002; V. Patrício et al. 2018). Furthermore, the ionization–metallicity relation is not constant across all redshifts, such that O2, O32, and Ne3O2 indices calibrated at a lower redshift tend to underestimate the metallicity for higher redshift sources (P. Garg et al. 2024; I. H. Laseter et al. 2024; R. L. Sanders et al. 2021, 2024). Indeed, M. Tang et al. (2019) and N. A. Reddy et al. (2023) find that the specific SFR (sSFR) and gas density may play more central roles than metallicity in modulating $\log U$ (and hence indices like O2, O32, and Ne3O2) at these redshifts. These indices tend to predict lower oxygen abundances for the 12 REBELS galaxies, with a maximum $12 + \log(\mathrm{O/H})$ of 8.4 (see Appendix C). We note that the N2 ratio also shows a monotonic relation with metallicity, and whilst it is has not yet been calibrated with high-z auroral line detections, the calibrations based on local analogues (K. Nakajima et al. 2022) are more consistent with the fiducial metallicities of the REBELS sample adopted in this work (see Table C3).

We have elected to use the R23 and R3 ratios for our fiducial metallicity estimates where possible (but use O32 for the three sources where the R3 and R23 calibrations have no real solution). We list the oxygen abundances derived using O32, Ne3O2, $\hat{R}$ (defined in I. H. Laseter et al. 2024), N2, and other indices for all the galaxies in our sample in Appendix C, and we also re-analyse the MZR and FMR based on these values therein. Due to the scatter in our sample, and in the literature, using these ratios does not significantly change the derived MZR and FMR, and we find that the REBELS galaxies still have oxygen abundances as much as ~ 0.4 dex higher than other galaxies at $6 < z < 8$. Therefore, whilst it is important to treat the absolute values with caution, it is clear that the REBELS galaxies are more metal-rich compared to most EoR galaxies in other existing spectroscopic surveys.

4.3 Star formation rate

Following, for example, K. E. Heintz et al. (2023a) and K. Nakajima et al. (2023), we use Hβ as an SFR tracer in lieu of the commonly used Hα luminosity, as an indicator for ongoing ($\sim$10 Myr) star formation activity. This choice is necessitated by the spectral coverage limitation of NIRSpec, which does not extend to Hα at redshifts $z \gtrsim 7$. This use of Hβ therefore allows us to maintain consistency in SFR measurements across our sample, and with measurements at high-z in the literature. The SFR is derived from the Hβ luminosity, $L_{\mathrm{H}\beta}$, assuming a P. Kroupa (2001) IMF following R. C. Kennicutt (1998):

$$\mathrm{SFR}_{\mathrm{H}\beta}(\mathrm{M}_\odot \mathrm{yr}^{-1}) = 5.37 \times 10^{-42} \times L_{\mathrm{H}\beta}(\mathrm{ergs}^{-1}) \times 2.86. \quad (8)$$

For the galaxies where we do not have attenuation-corrected Hβ luminosities, we determine lower limits to the SFR from the observed Hβ emission. We add that a comparison of the SFR of this sample from different tracers will be the focus of a subsequent paper (Fisher et al. 2025). When comparing with other galaxies in the literature, we apply a correction factor to their reported SFRs if other IMFs are used, so that the resulting SFRs are consistent with using a P. Kroupa (2001) IMF.

5 SED FITTING

We derive stellar masses for the REBELS galaxies using the BAGPIPES SED-fitting code (2016 version). We briefly outline our method here, with full details given in Stefanon et al. (in preparation). We use the G. Bruzual & S. Charlot (2003) stellar population models, which assume a P. Kroupa (2001) IMF. Nebular emission is modelled using CLOUDY (G. J. Ferland et al. 2017), assuming a spherical constant-density gas distribution with $n(H) = 100$ cm^{-3}, matching the metallicity of the stellar component. The metallicity priors for the SED fitting were Gaussian, centred on the metallicity estimates derived in this work, with the standard deviation reflecting the associated uncertainties. The redshifts were fixed to the value measured from the [C II]158 μm emission, accounting for small systematic shifts in the NIRSpec wavelengths (see Stefanon et al., in preparation). We adopted a D. Calzetti et al. (2000) attenuation curve, allowing the stellar dust attenuation ($A_{\mathrm{V},*}$, i.e. different to the nebular attenuation determined using the Balmer decrement in Section 3.1) to vary freely in the range 0−3 mag under a flat prior. For the SFH, we employed a non-parametric model with a continuity prior, designed to capture both recent bursts and early assembly phases. Other SFH parametrizations, including a constant + burst model, were also explored in Stefanon et al. (in preparation).

With this SED fitting, we find a range in stellar masses of $\log(M_*/\mathrm{M}_\odot) \sim 9.2 - 9.8$ (presented in Table 4). These stellar masses are slightly lower than those found for the same galaxies from non-parametric SED fitting in M. W. Topping et al. (2022). A full comparison of these different results will be presented in Stefanon et al. (in preparation). The continuum attenuation values derived from the SED fitting are lower than the nebular attenuation derived from the Balmer decrement, as expected for SF galaxies (e.g. D. Calzetti et al. 1994).

While the non-parametric approach provides flexibility in reconstructing the assembly history, the stellar mass measurements of these sources can still be impacted by the 'outshining' effect, where young, luminous stellar populations dominate the observed light, potentially causing a systematic underestimation of the stellar masses (e.g. C. Giménez-Arteaga et al. 2023). However, the impact of outshining is expected to diminish at higher stellar masses, as discussed in N. E. P. Lines et al. (2025). Dust obscuration can also present challenges when deriving stellar masses and other stellar population parameters. For the REBELS sources analysed here, it is likely that the observed light in the rest-frame UV/optical (as traced by these *JWST* observations) is primarily emitted by less-obscured regions. However, there may be fully obscured SF regions that do not emit at all in these wavelengths and are only detectable in the infrared. This results in an incomplete picture of the total stellar mass if only unobscured regions are traced. Such obscured regions are evident in some REBELS sources, where spatial offsets between UV/optical and infrared emission suggest the presence of highly obscured star formation (e.g. A. P. S. Hygate et al. 2023; L. E. Rowland et al. 2024a). Future spatially resolved SED analyses, including comparisons with high-resolution ALMA FIR data, will be critical for mitigating such uncertainties and providing more accurate estimates of the stellar mass distribution within these galaxies.

6 DISCUSSIONS

6.1 The mass–metallicity relation

With these observations of the REBELS galaxies, we are able to increase the sampling at the high-mass end of the MZR in SF galaxies during the EoR, since typical large-scale *JWST* surveys mainly contain galaxies with $\log(M_*/\mathrm{M}_\odot) < 9$. We make comparisons with observations at lower stellar mass, including a sample of galaxies from CEERS (S. L. Finkelstein et al. 2023), GLASS (G. Roberts-

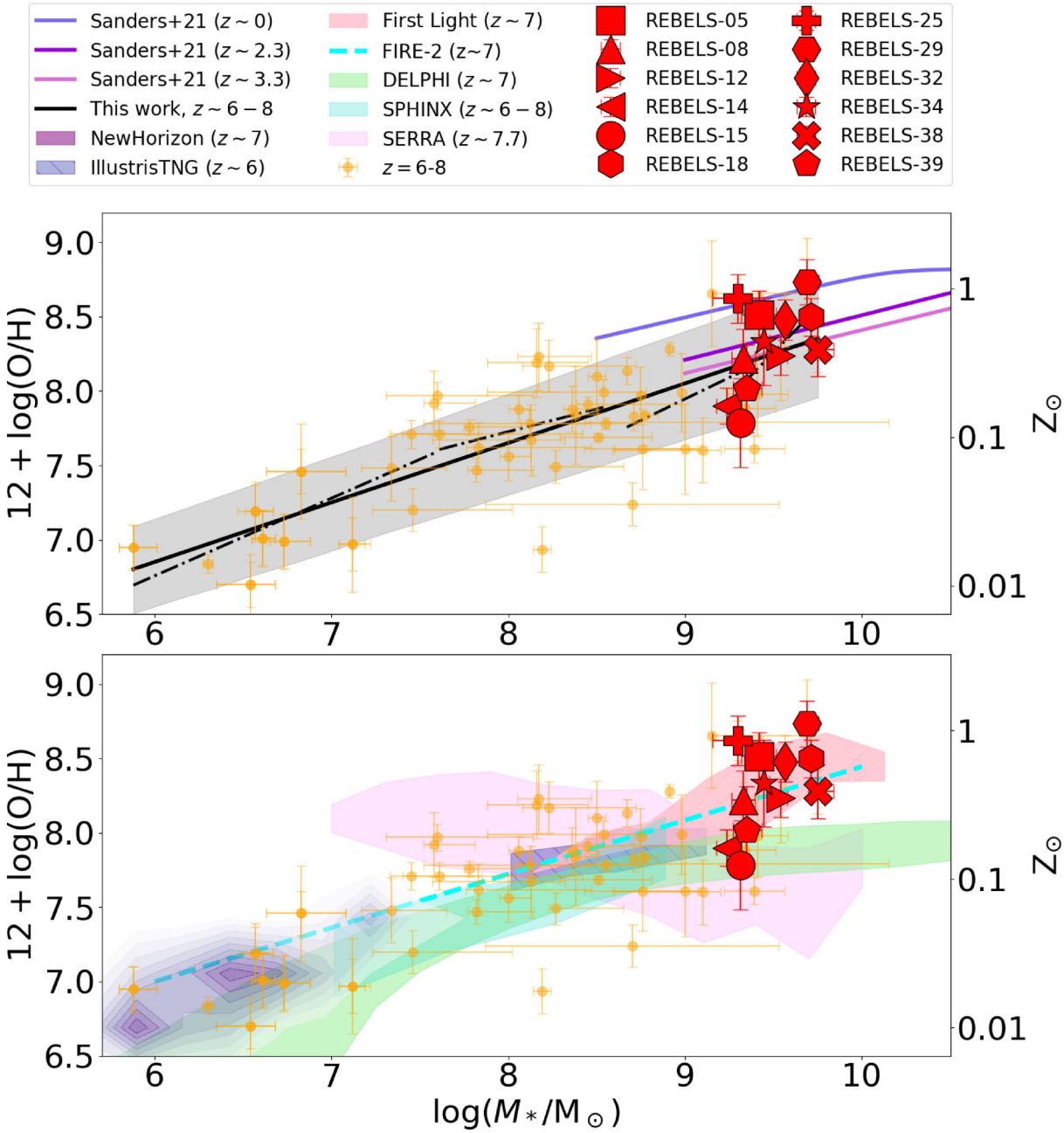

Figure 6. We show the MZR at $z = 6$–8 for the REBELS galaxies and sources from the literature (I. Chemerynska et al. 2024; K. Nakajima et al. 2023). In the top panel, the best-fitting MZR is indicated by the solid black line, with the 1σ uncertainty shown with the grey shaded area. We also plot the MZR at $z \sim 0$, ~ 2.3, and ~ 3.3 from R. L. Sanders et al. (2021) to investigate the redshift evolution of this scaling relation. The black dash–dotted lines show the best-fitting MZR in four mass bins, each with 15 galaxies, across this 4 dex range in stellar mass. In the bottom panel, we compare the MZR to theoretical predictions from NEWHORIZON (Y. Dubois et al. 2021), TNG100 (P. Torrey et al. 2019), FIRST LIGHT (Y. Nakazato, N. Yoshida & D. Ceverino 2023), FIRE-2 (A. Marszewski et al. 2024), DELPHI (Mauerhofer et al., in preparation), and SPHINX (H. Katz et al. 2023a). For FIRE-2, we plot the best-fitting MZR from the 'Slope and Normalization Evolution' model at $z = 7$. For FIRST LIGHT, TNG100, DELPHI, and SPHINX, we show the 16th–84th percentile distribution of these predictions by the coloured regions.

Borsani et al. 2024), some early release observation (ERO) programs collected and analysed in K. Nakajima et al. (2023), and from the UNCOVER (Ultradeep NIRSpec and NIRCam ObserVations before the Epoch of Reionization; R. Bezanson et al. 2024) program (analysed in I. Chemerynska et al. 2024). Selecting galaxies only in the redshift range of $6 < z < 8$, we have a sample of 49 galaxies with publicly available stellar masses, SFRs, and the relevant emission-line ratios to derive $12 + \log(\mathrm{O/H})$ with a consistent methodology using the R. L. Sanders et al. (2024) calibrations (i.e. [O III], Hβ, [O II], and/or an additional Balmer line). For the sources in I. Chemerynska et al. (2024), the R3 in R. L. Sanders et al. (2024) calibrations were already used to determine the oxygen abundance. For the K. Nakajima et al. (2023) sources, the K. Nakajima et al. (2022) calibrations were used. To be consistent, we recalibrate the

K. Nakajima et al. (2023) sources using the R. L. Sanders et al. (2024) calibrations, following the methodology outlined in Section 4.2. However, we note that the main findings of this analysis are consistent even if we use the K. Nakajima et al. (2022) R3 or R23 calibrations for all the sources.

We plot the MZR for the 12 REBELS galaxies, and the literature sources at $z \sim 6-8$, in Fig. 6. Here, we see that *JWST* observations in this redshift range span around 4 dex of stellar mass, and the addition of the REBELS galaxies more than doubles the number of galaxies at $z > 6$ with $M_* > 10^9\,M_\odot$ in comparison to other recent MZR studies (K. E. Heintz et al. 2023a; K. Nakajima et al. 2023; M. Curti et al. 2024; A. Sarkar et al. 2025).

Following R. L. Sanders et al. (2021), we fit the MZR using:

$$12 + \log(\mathrm{O/H}) = \gamma \log(\frac{M_*}{10^{10}\mathrm{M}_\odot}) + Z_{10} \quad (9)$$

and find a best-fitting slope with $\gamma = 0.37 \pm 0.03$ and $Z_{10} = 8.30 \pm 0.04$, with a 1σ scatter of 0.26 dex. We plot the best-fitting linear relation for the MZR as a solid black line in the top panel of Fig. 6, with the grey shaded region representing the uncertainty in the best fit. In this top panel, we also plot the MZR relation at lower redshifts from R. L. Sanders et al. (2021) at $z \sim 0$, ~ 2.3, and ~ 3.3, although we note that these metallicities are calculated with a χ^2-minimization using O32, Ne3O2, and R3 ratios. We find that the fitted MZR at $z = 6$–8 is consistent with the MZR reported in K. E. Heintz et al. (2023a) based on a different sample selection ($\gamma = 0.33$ at $z = 7$–10) and from I. Chemerynska et al. (2024; $\gamma = 0.39$ at $z = 6$–8). The latter study was based on a similar sample to the one analysed here (excluding the REBELS sources) but did not apply a consistent metallicity calibration methodology across the full sample, as done in this work. However, these MZR slopes are steeper than those found in M. Curti et al. (2024); K. Nakajima et al. (2023); and A. Sarkar et al. (2025) at $z > 4$. We also find that this best-fitting MZR at $z = 6$–8 is steeper than the lower redshift MZRs reported in R. L. Sanders et al. (2021). As aforementioned, there is some caution to be taken in comparing these different fitted MZRs, since different works use different SED fitting parameters and metallicity calibrations. We show in Appendix C that using the O32 ratio for this sample results in slightly lower $\gamma = 0.27 \pm 0.07$ and $Z_{10} = 8.17 \pm 0.08$, but this best fit is still consistent within the uncertainties.

Whilst most MZR studies at $z > 2$ find that oxygen abundances at a given M_* are significantly lower at high-z, the REBELS galaxies lie in a similar parameter space as the lower-z (and even $z \sim 0$) relations, although we note that there is significant scatter within the sample. This alignment could be attributed to the observed flattening of the MZR at high masses at $z \sim 0$, with a characteristic turnover mass around $\log(M_0/\mathrm{M}_\odot) \sim 10$ (M. Curti et al. 2020). This flattening is often attributed either to the advanced stage of chemical evolution in massive galaxies, a phenomenon known as 'chemical downsizing' (R. S. Somerville & R. Davé 2015), or to the enhanced ability of massive galaxies to retain metals due to their deep gravitational wells. In contrast, lower mass galaxies more readily lose enriched gas via outflows and winds (e.g. J. Chisholm et al. 2015). The MZR turnover occurs when gas-phase oxygen levels become high enough that a significant fraction of oxygen is locked in low-mass stars. This turnover mass, M_0, is roughly where the stellar-to-gas mass ratio is unity, or equivalently, where the gas fraction $f_{\rm gas} \sim 0.5$ (H. J. Zahid et al. 2014). The turnover mass has been found to increase with increasing redshift out to $z \sim 1.5$ (H. J. Zahid et al. 2014), with indications that this is also true out to $z \sim 2.3$ (R. L. Sanders et al. 2021). To tentatively assess whether there is any flattening of the MZR in this sample of $z = 6$–8 galaxies, we create four bins of 15 galaxies according to their stellar mass, and recalculate the MZR in each bin according to equation (9). The slopes for each mass bin are indicated by the black dash–dotted lines in the top panel of Fig. 6. With this sample of $6 \lesssim \log(M_*/\mathrm{M}_\odot) \lesssim 10$ galaxies at $z = 6$–8, we see no evidence of the MZR flattening at the high-mass end, although we note there is significant scatter. Indeed, from the [C II]-based gas masses and derived gas fractions (M. Aravena et al. 2024; H. Algera et al. 2025) of the REBELS sample, all the gas fractions are > 0.61, indicating that, if the flattening of the MZR does persist out to these redshifts, we may not have yet reached the turnover mass ($M_0(z \sim 7) > 10^{10}\mathrm{M}_\odot$). However, as discussed in Section 5, integrated SED fitting can underestimate the derived stellar masses by as much as ~ 0.5 dex (e.g. C. Giménez-Arteaga et al. 2023) due to the 'outshining' effect, which may particularly be a problem for the REBELS galaxies, based on the finding that they may be more evolved systems with potentially older stellar populations that are outshone by the emission from brighter, younger stellar populations. Spatially resolved SED fitting of the REBELS galaxies in subsequent works will be able to assess this effect on the derived slope of the MZR in more detail.

In I. Chemerynska et al. (2024), the scatter in the MZR at $z \sim 6$–8 is found to increase at lower stellar masses, interpreted as due to more stochastic star formation and ISM enrichment at these low masses. With the recalibrated sample presented here, we find a relatively consistent scatter of ~ 0.25 dex across the four mass bins from $\log(M_*/\mathrm{M}_\odot) = 6$ to 10. This scatter is significantly higher than the ~ 0.1 dex scatter typically found at low redshifts (e.g. B. H. Andrews & P. Martini 2013), and is consistent with the MZR scatter from the SERRA simulations at $z \sim 7$ (A. Pallottini et al. 2025). This scatter is also consistent with the analytic models described in A. Pallottini et al. (2025) with a weak supernova feedback efficiency ($\epsilon_{\rm SN} = 1/4$) and a low-amplitude SFR flickering ($\sigma_{\rm SFR} \approx 0.2$), resulting in an intrinsic scatter of ~ 0.25 dex at $z = 3 - 10$. However, we note that the scatter in the REBELS sample, as well as other literature samples at high-z, may be affected by other intrinsic or systematic effects, such as systematics in the metallicity calibrations used, systematics in the stellar mass estimates, contamination from AGN, and effects from galaxy interactions/mergers.

In the bottom panel of Fig. 6, we also compare the observed MZR with predictions from cosmological simulations at $z \sim 7$, including from NEWHORIZON (Y. Dubois et al. 2021), TNG100 (P. Torrey et al. 2019), FIRST LIGHT (Y. Nakazato et al. 2023), FIRE-2 (A. Marszewski et al. 2024), SPHINX (H. Katz et al. 2023a), and SERRA (A. Pallottini et al. 2025). We also plot for comparison the predictions from the semi-analytical model, DELPHI (Mauerhofer et al. in preparation, see also V. Mauerhofer & P. Dayal 2023), which incorporates cold gas fractions and star-formation efficiencies derived from the SPHINX simulation. Where necessary, we have scaled these relations to a P. Kroupa (2001) IMF and a solar metallicity of $12 + \log(\mathrm{O/H}) = 8.69$ (M. Asplund et al. 2009). Across these different simulations, the slopes at $\log(M_*/\mathrm{M}_\odot) \sim 7.5$–8.5 are broadly consistent. Comparisons with these predictions at the low-mass end ($\log(M_*/\mathrm{M}_\odot) \lesssim 8$) are detailed in I. Chemerynska et al. (2024), and here we focus on the high-mass end populated by the REBELS sources ($\log(M_*/\mathrm{M}_\odot) \sim 9$–10), where there are some variations in the predicted slope and normalization of the MZR.

In particular, FIRST LIGHT and FIRE-2 predict similarly metal-rich, massive galaxies at these redshifts, consistent with the observations of the REBELS sample, although we note that both of these predictions show the redshift evolution of selected massive galaxies from zoom-in simulations, whilst for the other simulations the median and/or 1σ distribution of the MZR for the full sample within

the large volume of the simulations are reported at each analysed redshift in the corresponding papers, which typically contain few massive ($\log(M_*/\mathrm{M}_\odot) \gtrsim 9$) galaxies at $z > 6$. In A. Marszewski et al. (2024), from which we plot the best-fitting MZR from the 'Slope and Normalization Evolution' model at $z = 7$, 34 massive galaxies from FIRE-2 (X. Ma et al. 2018, 2019) are selected for zoom-in simulations run down to either $z = 5$, 7, or 9, with halo masses $\sim 10^9$-$10^{12}\mathrm{M}_\odot$ at these final redshifts. In Y. Nakazato et al. (2023), from which we plot the 5–95 per cent dispersion in the sample at $z = 7$, 62 galaxies are selected from the FIRST LIGHT simulation suite (D. Ceverino, S. C. O. Glover & R. S. Klessen 2017) with maximum circular velocities > 178 km s^{-1} at $z = 5$. Differences in feedback prescriptions and stellar yields may also contribute to variations, and we add there may be other systematic differences in the way each simulation derives the stellar masses and metallicities. For example, the mass-weighted metallicity is given for FIRE-2 and NEWHORIZON. However, in FIRST LIGHT, SPHINX, and TNG100, the gas-phase metallicities are weighted by either [O III] line luminosity or SFR. This likely makes their predictions more comparable to observations, which are only sensitive to the bright, line-emitting star-forming regions.

A full assessment of the systematic differences between different simulations is beyond the scope of this work, but overall the consistency with simulations like FIRST LIGHT and FIRE-2 supports the idea that massive galaxies in the reionization era could reach relatively high metallicities in a short time-scale. These findings align with a scenario where substantial chemical evolution occurs early and rapidly in massive galaxies, within just a few hundred million years.

6.2 The fundamental metallicity relation

To address the scatter in the $z = 0$ MZR, the SFR was introduced as an additional variable in what is known as the FMR (e.g. S. L. Ellison et al. 2008; M. A. Lara-López et al. 2010; F. Mannucci et al. 2010), where $12 + \log(\mathrm{O/H})$ decreases with increasing SFR at fixed M_*. As with, for example, K. Nakajima et al. (2023), we use the following to define the FMR:

$$\mu_\alpha = \log(M_*/\mathrm{M}_\odot) - \alpha \log(\mathrm{SFR}/\mathrm{M}_\odot \mathrm{yr}^{-1}), \quad (10)$$

where $\alpha = 0.66$ is found to minimize the scatter in the FMR at $z \sim 0$ in B. H. Andrews & P. Martini (2013, solid blue line in Fig. 7).

The FMR has been found to be largely redshift invariant out to $z \sim 4$ (e.g. M. Curti et al. 2020, 2023; K. E. Heintz et al. 2023a; A. Henry et al. 2013, 2021; D. Langeroodi et al. 2023; K. Nakajima et al. 2023; R. L. Sanders et al. 2021). At $z > 4$, however, recent studies have found a deviation in the observed FMR, although the exact redshift at which the observations deviate from the $z \sim 0$ FMR differs across the literature (e.g. $z \sim 7$ in K. E. Heintz et al. 2023a, $z \sim 8$ in K. Nakajima et al. 2023, $z \sim 6$ in M. Curti et al. 2024, $z \sim 4$ in D. Langeroodi et al. 2023). These studies find that high-z galaxies are more metal-poor than the $z \sim 0$ FMR predicts, however with a poor sampling of high-mass galaxies out to higher redshifts. With the REBELS galaxies observed here, we extend this study to more massive EoR galaxies.

In Fig. 7, we find that the REBELS galaxies studied in this work typically exhibit higher values of $\mu_{0.66}$, which corresponds to lower sSFR compared to other $6 < z < 8$ galaxies in the literature. These REBELS sources are also scattered above and below the $z \sim 0$ FMR, whereas most of the literature sample lies below it. This could suggest that the predominantly negative FMR offsets reported for high-z galaxies may partially reflect a selection bias in current studies, which often target low-mass, metal-poor galaxies with high sSFRs and [O III] EWs that may be more likely to show negative residuals relative to the local FMR.

Extreme line emitters, characterized by large [O III] EWs and high sSFRs, may be more likely to show negative residuals relative to the FMR because their ISM conditions deviate significantly from the typical balance of star formation, metallicity, and gas content seen in the local Universe. These systems likely experience recent bursts of star formation that dominate the observed spectra, amplifying the appearance of low metallicity and high ionization regions.

Another plausible explanation for a negative offset to the FMR at high-z is significant accretion of pristine gas from the IGM at these redshifts, which dilutes the chemical abundances in the ISM and causes galaxies to be more metal-poor than the FMR predicts (K. E. Heintz et al. 2023a). In this scenario, the REBELS galaxies could represent a more evolved population that, despite their high-gas masses and fractions ($\log M_{\mathrm{gas}}/\mathrm{M}_\odot = 9.7$–$10.7$, $f_{\mathrm{gas}} = 0.73$–0.96, H. Algera et al. 2025) indicative of ongoing accretion, earlier bursts of star formation may have already efficiently built up their stellar mass and enriched their ISM. Currently, only galaxies in the REBELS sample and a handful of other massive $z > 6$ galaxies have independent measurements of both gas mass ([CII]-based) and metallicity (e.g. RXCJ0600-z6.3 at $z = 6.072$ from S. Fujimoto et al. 2025; F. Valentino et al. 2024; S04950 at $z = 8.50$ from K. E. Heintz et al. 2023b; S. Fujimoto et al. 2024; and MACS1149-JD1 at $z = 9.11$ from N. Laporte et al. 2019; T. Morishita et al. 2025), significantly limiting investigations into the role of gas accretion in shaping the FMR at these redshifts. To distinguish between these possibilities, a larger sample of high-z galaxies with robust measurements of gas mass, metallicity, stellar mass, and SFR – particularly more gas mass estimates for low-mass systems – would be essential.

We also caution that there are various systematics in determining these properties, and we note that the B. H. Andrews & P. Martini (2013) $z \sim 0$ FMR is derived from direct method metallicities, although the conclusions are consistent when using the FMR from metallicities derived using strong-line methods in R. L. Sanders et al. (2021), as well as alternative formulations such as that of M. Curti et al. (2020). In addition to the caveats already discussed for deriving the oxygen abundance (Section 4.2.1), we were also unable to determine a nebular attenuation for four of the REBELS galaxies (white markers), which means that current estimates of the SFR from the uncorrected Hβ luminosity can only be taken as lower limits, whilst it is also possible that their stellar masses could be underestimated due to degeneracies between stellar mass, age, and interstellar reddening.

7 SUMMARY AND CONCLUSIONS

In this work, we have investigated the emission-line diagnostics and ionized gas properties of a sample of 12 massive EoR galaxies at $z = 6.496$ to 7.675 selected from the REBELS ALMA large program, observed with the *JWST* NIRSpec/IFU in the prism mode. Our findings reveal that the REBELS galaxies exhibit low O2, O32, and Ne3O2 ratios compared to other high-z galaxies from pre-existing large surveys, suggesting distinct ISM conditions and less intense ionizing fields. Recent *JWST* observations frequently identify galaxies with high O32 ratios (indicative of low metallicities), as these samples are often biased toward sources with extreme [O III] EWs. By contrast, the REBELS sources have [O III] EWs more comparable to the median of 450 Å at $z \sim 7$ (I. Labbé et al. 2013), enabling a more representative sampling of the ISM conditions of the general galaxy population at high redshift.

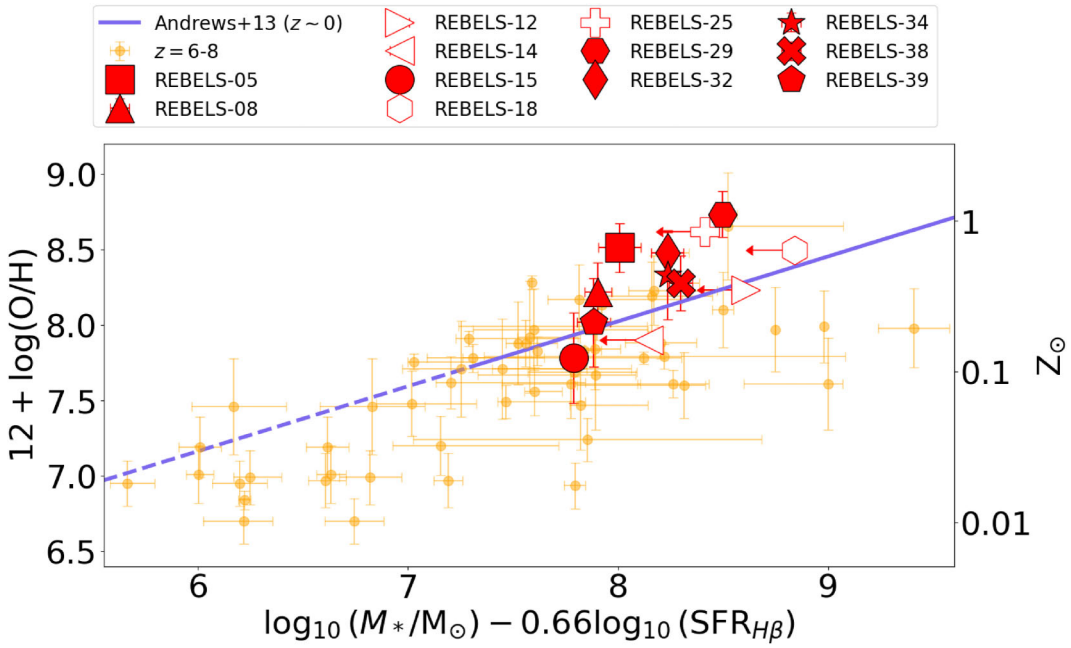

Figure 7. We plot the FMR for the REBELS galaxies and the literature sample at $z = 6$–8 (K. Nakajima et al. 2023; I. Chemerynska et al. 2024). We compare to the $z \sim 0$ FMR from B. H. Andrews & P. Martini (2013; solid blue line, extrapolated to $\mu_{0.66} < 7.3$ with the dashed line). White-filled markers indicate the REBELS galaxies where $SFR_{H\beta}$ is not attenuation-corrected, and is therefore a lower limit.

To derive the metallicities of our sample, we investigated a variety of strong-line indices and calibrations, and adopt the R. L. Sanders et al. (2024) calibrations based on 46 auroral line detections at $z > 2$ for our fiducial estimates. We predominantly used the R23 index, but used R3 where the fluxes could not be attenuation-corrected (for four galaxies where Hα is redshifted out of the NIRSpec coverage), and used O32 where the R23 index provides no real solution (for three galaxies that show elevated R3 and R23 ratios). These calibrations reveal a median metallicity of $\sim 0.4 Z_\odot$, with five REBELS galaxies having $Z_{gas} \gtrsim 0.5 Z_\odot$. Using O2, O32, and Ne3O2 ratios to derive the oxygen abundance tends to result in lower oxygen abundances for this sample, which may be due to the primary dependence of these ratios on other properties such as the ionization parameter, electron density, and sSFR. However, abundances derived using these indices still result in the REBELS galaxies being more metal-rich than the bulk of the $z > 6$ population in the literature (but see e.g. A. E. Shapley et al. 2025). The discrepancies found across different calibrations call for a further study of metallicity calibrations at high-z, and in particular calls for an increase in auroral line detections at higher metallicities.

The existence of metal-rich galaxies in the early Universe provides key insights into the rapid evolution of galaxies during the EoR. The REBELS sample suggests that some high-mass galaxies at $z \gtrsim 6$ exhibit relatively high metallicities, indicating that metal enrichment can rapidly occur within a few hundred million years of the big bang. Supporting this notion, a handful other galaxies from the reionization era have also been found to display similarly low O32 ratios (M. Killi et al. 2023; A. E. Shapley et al. 2025; C. Witten et al. 2025), and several recent studies have identified evolved stellar populations at $z \gtrsim 6$ (e.g. A. Kuruvanthodi et al. 2024). In addition, results from the FIRST LIGHT (Y. Nakazato et al. 2023) and FIRE-2 (A. Marszewski et al. 2024) simulations indicate that some massive galaxies can be enriched to near-solar abundances at these early cosmic times. These findings hint at a potentially non-negligible population of evolved galaxies within the EoR, suggesting that some galaxies may have experienced significant metal enrichment and advanced stages of stellar evolution much earlier than previously expected.

By compiling literature results from lower mass samples at the same redshift ($z = 6$–8), we analysed the MZR and FMR over a ~ 4 dex range in stellar mass. Notably, the REBELS galaxies significantly improve the sampling of the high-mass end of the MZR, more than doubling the number of massive ($\log(M_*/M_\odot) > 9$) SF galaxies with metallicity estimates at $z > 6$. The best-fitting MZR derived, with a slope of $\gamma = 0.37 \pm 0.03$, is consistent with some previous studies at $z > 6$ (e.g. K. E. Heintz et al. 2023a; I. Chemerynska et al. 2024) and is steeper than some studies at lower redshifts (e.g. R. L. Sanders et al. 2021). However, we note that systematic differences in the derivation of stellar masses, oxygen abundances, and SFRs across the literature may impact these comparisons.

For the FMR, the REBELS galaxies show a mix of positive and negative offsets relative to the $z = 0$ relation, in contrast to the predominantly negative offsets reported for lower mass, metal-poor galaxies in other high-z studies. This distinction may arise from a selection bias in current $z > 6$ samples, which often target extreme line emitters. These negative offsets may reflect significant accretion of pristine gas from the IGM, diluting ISM metallicities, and driving galaxies below the $z = 0$ FMR. In this context, the REBELS galaxies could represent a more evolved population that has already undergone substantial enrichment through early efficient star formation while maintaining high gas fractions indicative of ongoing accretion. These findings highlight the need for a larger, more diverse sample of $z = 6$–8 galaxies with robust measurements of stellar mass, gas mass, SFR, and metallicity to disentangle the effects of sample selection, ISM conditions, and galaxy evolution on the observed MZR and FMR at these redshifts.

ACKNOWLEDGEMENTS

We thank the referee for their useful comments and suggestions that significantly improved the clarity of this work. The authors would like to thank Alice Shapley for extensive discussions on high-z metallicity calibrations. The authors would also like to thank Elisa Cataldi for discussions on metallicity calibrations with *JWST* data. LR acknowledges a grant from the Leiden University Fund/Bouwens Astrophysics Fund, www.luf.nl. MA acknowledges support from ANID Basal Project FB210003 and ANID MILENIO NCN2024_112. HA and HI acknowledge support from the NAOJ ALMA Scientific Research Grant Code 2021–19A. AF acknowledges support from the ERC Advanced Grant INTERSTELLAR H2020/740120. JH acknowledges support from the ERC Consolidator Grant 101088676 (VOYAJ). PD warmly thanks the European Commission's and University of Groningen's CO-FUND Rosalind Franklin program. VG gratefully acknowledges support from ANID/CONICYT + FONDECYT Regular 1221310 and by the ANID BASAL project FB210003.

This work is based on observations made with the NASA/ESA/CSA *JWST*. The data were obtained from the Mikulski Archive for Space Telescopes at the Space Telescope Science Institute, which is operated by the Association of Universities for Research in Astronomy, Inc., under NASA contract NAS 5–03127 for *JWST*. These observations are associated with programs nos 1626 and 2659.

This paper made use of the following software packages: ASTROPY (Astropy Collaboration 2022), MATPLOTLIB (J. D. Hunter 2007), NUMPY (C. R. Harris et al. 2020), SCIPY (P. Virtanen et al. 2020), SPECTRAL-CUBE (A. Ginsburg et al. 2019), APLPY (T. Robitaille & E. Bressert 2012), and ASTRODENDRO (http://www.dendrograms.org/).

DATA AVAILABILITY

The data used in this manuscript will be made available upon reasonable request to the corresponding author.

REFERENCES

Algera H. et al., 2024, MNRAS, 533, 3098
Algera H. et al., 2025, preprint (arXiv:2501.10508)
Algera H. S. B. et al., 2024, MNRAS, 527, 6867
Andrews B. H., Martini P., 2013, ApJ, 765, 140
Aravena M. et al., 2024, A&A, 682, A24
Arellano-Córdova K. Z. et al., 2022, ApJ, 940, L23
Asplund M., Grevesse N., Sauval A. J., Scott P., 2009, ARA&A, 47, 481
Astropy Collaboration, 2022, ApJ, 935, 167
Backhaus B. E. et al., 2022, ApJ, 926, 161
Baldwin J. A., Phillips M. M., Terlevich R., 1981, PASP, 93, 5
Bañados E. et al., 2018, Nature, 553, 473
Bezanson R. et al., 2024, ApJ, 974, 92
Bian F., Kewley L. J., Dopita M. A., 2018, ApJ, 859, 175
Bouwens R. J. et al., 2022, ApJ, 931, 160
Brammer G., 2023, Zenodo
Brinchmann J., 2023, MNRAS, 525, 2087
Bruzual G., Charlot S., 2003, MNRAS, 344, 1000
Bunker A. J. et al., 2023, A&A, 677, A88
Calzetti D., Armus L., Bohlin R. C., Kinney A. L., Koornneef J., Storchi-Bergmann T., 2000, ApJ, 533, 682
Calzetti D., Kinney A. L., Storchi-Bergmann T., 1994, ApJ, 429, 582
Cameron A. J. et al., 2023, A&A, 677, A115
Cardelli J. A., Clayton G. C., Mathis J. S., 1989, ApJ, 345, 245
Carnall A. C. et al., 2023, MNRAS, 518, L45
Carniani S. et al., 2024, Nature, 633, 318
Casey C. M. et al., 2024, ApJ, 965, 98
Castellano M. et al., 2022, ApJ, 938, L15
Cataldi E., et al. 2025. Astronomy & Astrophysics, 703, A208
Ceverino D., Glover S. C. O., Klessen R. S., 2017, MNRAS, 470, 2791
Chabrier G., 2003, PASP, 115, 763
Chemerynska I. et al., 2024, ApJ, 976, L15
Chisholm J., Tremonti C. A., Leitherer C., Chen Y., Wofford A., Lundgren B., 2015, ApJ, 811, 149
Curti M. et al., 2022, MNRAS, 518, 425
Curti M. et al., 2023, MNRAS, 518, 425
Curti M. et al., 2024, A&A, 684, A75
Curti M., Cresci G., Mannucci F., Marconi A., Maiolino R., Esposito S., 2017, MNRAS, 465, 1384
Curti M., Mannucci F., Cresci G., Maiolino R., 2020, MNRAS, 491, 944
D'Eugenio F. et al., 2025, ApJS, 277, 4
Díaz A. I., Castellanos M., Terlevich E., Luisa García-Vargas M., 2000, MNRAS, 318, 462
Dopita M. A., Sutherland R. S., 2003, Astrophysics of the Diffuse Universe. Astronomy and Astrophysics Library, Springer, Berlin, Heidelberg
Dubois Y. et al., 2021, A&A, 651, A109
Eisenstein D. J. et al., 2023, Overview of the JWST Advanced Deep Extragalactic Survey (JADES)
Ellison S. L., Patton D. R., Simard L., McConnachie A. W., 2008, ApJ, 672, L107
Ferland G. J. et al., 2013, Rev. Mex. Astron. Astrofis., 49, 137
Ferland G. J. et al., 2017, Rev. Mex. Astron. Astrofis., 53, 385
Finkelstein S. L. et al., 2023, ApJ, 946, L13
Fisher R. et al., 2025, MNRAS, 539, 109
Fitzpatrick E. L., 1999, PASP, 111, 63
Fujimoto S. et al., 2024, ApJ, 964, 146
Fujimoto S. et al., 2025, Nat. Astron., 9, 1553
Garg P., Narayanan D., Sanders R. L., Davé R., Popping G., Shapley A. E., Stark D. P., Trump J. R., 2024, ApJ, 972, 113
Giménez-Arteaga C. et al., 2023, ApJ, 948, 126
Ginsburg A. et al., 2019, radio-astro-tools/spectral-cube: v0.4.4, Zenodo
Ginsburg A., Sokolov V., de Val-Borro M., Rosolowsky E., Pineda J. E., Sipőcz B. M., Henshaw J. D., 2022, AJ, 163, 291
Gutkin J., Charlot S., Bruzual G., 2016, MNRAS, 462, 1757
Harris C. R. et al., 2020, Nature, 585, 357
Hashimoto T. et al., 2018, Nature, 557, 392
Heintz K. E. et al., 2023a, Nat. Astron., 7, 1517
Heintz K. E. et al., 2023b, ApJ, 944, L30
Heintz K. E. et al., 2025, A&A, 693, A60
Henry A. et al., 2013, ApJ, 776, L27
Henry A. et al., 2021, ApJ, 919, 143
Hsiao T. Y.-Y. et al., 2025, ApJ, 993, 70
Hummer D. G., Storey P. J., 1987, MNRAS, 224, 801
Hunter J. D., 2007, Comput. Sci. Eng., 9, 90
Hygate A. P. S. et al., 2023, MNRAS, 524, 1775
Inami H. et al., 2022, MNRAS, 515, 3126
Jones T., Sanders R., Roberts-Borsani G., Ellis R. S., Laporte N., Treu T., Harikane Y., 2020, ApJ, 903, 150
Katz H. et al., 2023a, Open J. Astrophys., 6
Katz H. et al., 2023b, MNRAS, 518, 592
Kauffmann G. et al., 2003, MNRAS, 346, 1055
Kennicutt R. C., Jr, 1998, ApJ, 498, 541
Kewley L. J., Dopita M. A., 2002, ApJS, 142, 35
Kewley L. J., Dopita M. A., Sutherland R. S., Heisler C. A., Trevena J., 2001, ApJ, 556, 121
Kewley L. J., Ellison S. L., 2008, ApJ, 681, 1183
Kewley L. J., Nicholls D. C., Sutherland R., Rigby J. R., Acharya A., Dopita M. A., Bayliss M. B., 2019, ApJ, 880, 16
Killi M. et al., 2023, MNRAS, 521, 2526
Kroupa P., 2001, MNRAS, 322, 231
Kuruvanthodi A., Schaerer D., Marques-Chaves R., Korber D., Weibel A., Oesch P., Roberts-Borsani G., 2024, A&A, 691, A310
Labbé I. et al., 2013, ApJ, 777, L19
Langeroodi D. et al., 2023, ApJ, 957, 39

Langeroodi D., Hjorth J., 2024, Genesis-Metallicity: Universal Non-Parametric Gas-Phase Metallicity Estimation
Laporte N. et al., 2019, MNRAS, 487, L81
Lara-López M. A. et al., 2010, A&A, 521, L53
Laseter I. H. et al., 2024, A&A, 681, A70
Lilly S. J., Carollo C. M., Pipino A., Renzini A., Peng Y., 2013, ApJ, 772, 119
Lines N. E. P. et al., 2025, MNRAS, 539, 2685
Liu X., Shapley A. E., Coil A. L., Brinchmann J., Ma C.-P., 2008, ApJ, 678, 758
Ma X. et al., 2018, MNRAS, 478, 1694
Ma X. et al., 2019, MNRAS, 487, 1844
Maiolino R. et al., 2008, A&A, 488, 463
Maiolino R., Mannucci F., 2019, A&AR, 27, 3
Mannucci F., Cresci G., Maiolino R., Marconi A., Gnerucci A., 2010, MNRAS, 408, 2115
Marrone D. P. et al., 2018, Nature, 553, 51
Marszewski A., Sun G., Faucher-Giguère C.-A., Hayward C. C., Feldmann R., 2024, ApJ, 967, L41
Mascia S. et al., 2023, A&A, 672, A155
Mauerhofer V., Dayal P., 2023, MNRAS, 526, 2196
Mollá M., García-Vargas M. L., Bressan A., 2009, MNRAS, 398, 451
Morishita T. et al., 2025, ApJ, 982, 153
Moustakas J., Kennicutt R. C., Jr, Tremonti C. A., Dale D. A., Smith J.-D. T., Calzetti D., 2010, ApJS, 190, 233
Naidu R. P. et al., 2022, ApJ, 940, L14
Nakajima K. et al., 2022, ApJS, 262, 3
Nakajima K., Ouchi M., Isobe Y., Harikane Y., Zhang Y., Ono Y., Umeda H., Oguri M., 2023, ApJS, 269, 33
Nakazato Y., Yoshida N., Ceverino D., 2023, ApJ, 953, 140
Narayanan D. et al., 2025, ApJ, 982, 7
Osterbrock D. E., Ferland G. J., 2006, Astrophysics of Gaseous Nebulae and Active Galactic Nuclei. University Science Books, Sausalito, CA
Pallottini A., Ferrara A., Gallerani S., Sommovigo L., Carniani S., Vallini L., Kohandel M., Venturi G., 2025, A&A, 699, A6
Papovich C. et al., 2022, ApJ, 937, 22
Patrício V., Christensen L., Rhodin H., Cañameras R., Lara-López M. A., 2018, MNRAS, 481, 3520
Peeples M. S., Shankar F., 2011, MNRAS, 417, 2962
Pérez-Montero E., 2014, MNRAS, 441, 2663
Pirzkal N. et al., 2024, ApJ, 969, 90
Reddy N. A., Topping M. W., Sanders R. L., Shapley A. E., Brammer G., 2023, ApJ, 952, 167
Rhoads J. E. et al., 2023, ApJ, 942, L14
Roberts-Borsani G. et al., 2024, ApJ, 976, 193
Roberts-Borsani G. W. et al., 2016, ApJ, 823, 143
Robertson B. E. et al., 2023, Nat. Astron., 7, 611
Robitaille T., Bressert E., 2012, Astrophysics Source Code Library, record ascl:1208.017
Rowland L. E. et al., 2024a, MNRAS, 535, 2068
Rowland L. E. et al., 2024b, A&A, 685, A46
Sanders R. L. et al., 2021, ApJ, 914, 19
Sanders R. L., Shapley A. E., Topping M. W., Reddy N. A., Brammer G. B., 2023, ApJ, 955, 54
Sanders R. L., Shapley A. E., Topping M. W., Reddy N. A., Brammer G. B., 2024, ApJ, 962, 24
Sarkar A. et al., 2025, ApJ, 978, 136
Scarlata C., Hayes M., Panagia N., Mehta V., Haardt F., Bagley M., 2024, On the universal validity of Case B recombination theory, preprint (arXiv:2404.09015)
Schady P. et al., 2024, MNRAS, 529, 2807
Schaerer D., Marques-Chaves R., Barrufet L., Oesch P., Izotov Y. I., Naidu R., Guseva N. G., Brammer G., 2022, A&A, 665, L4
Scholtz J. et al., 2025, A&A, 697, A175
Schouws S. et al., 2022, ApJ, 928, 31
Schouws S. et al., 2025, ApJ, 988, 19
Shapley A. E. et al., 2015, ApJ, 801, 88
Shapley A. E. et al., 2025, ApJ, 981, 167
Shapley A. E., Coil A. L., Ma C.-P., Bundy K., 2005, ApJ, 635, 1006
Somerville R. S., Davé R., 2015, ARA&A, 53, 51
Steidel C. C. et al., 2014, ApJ, 795, 165
Storey P. J., Zeippen C. J., 2000, MNRAS, 312, 813
Strandet M. L. et al., 2017, ApJ, 842, L15
Strom A. L., Steidel C. C., Rudie G. C., Trainor R. F., Pettini M., 2018, ApJ, 868, 117
Strom A. L., Steidel C. C., Rudie G. C., Trainor R. F., Pettini M., Reddy N. A., 2017, ApJ, 836, 164
Tamura Y. et al., 2019, ApJ, 874, 27
Tang M. et al., 2023, MNRAS, 526, 1657
Tang M., Stark D. P., Chevallard J., Charlot S., 2019, MNRAS, 489, 2572
Tarter C. B., Tucker W. H., Salpeter E. E., 1969, ApJ, 156, 943
Taylor A. J., Barger A. J., Cowie L. L., 2022, ApJ, 939, L3
Topping M. W. et al., 2022, MNRAS, 516, 975
Torrey P. et al., 2019, MNRAS, 484, 4
Tremonti C. A. et al., 2004, ApJ, 613, 898
Treu T. et al., 2022, ApJ, 935, 110
Trump J. R. et al., 2023, ApJ, 945, 35
Übler H. et al., 2023, A&A, 677, A145
Valentino F. et al., 2024, A&A, 685, A138
van Dokkum P. G., 2001, PASP, 113, 1420
Veilleux S., Osterbrock D. E., 1987, The Astrophysical Journal Supplement Series, 63, 295
Venturi G. et al., 2024, A&A, 691, A19
Virtanen P. et al., 2020, Nat. Methods, 17, 261
Watson D., Christensen L., Knudsen K. K., Richard J., Gallazzi A., Michałowski M. J., 2015, Nature, 519, 327
Witten C. et al., 2025, MNRAS, 537, 112
Zahid H. J., Dima G. I., Kudritzki R.-P., Kewley L. J., Geller M. J., Hwang H. S., Silverman J. D., Kashino D., 2014, ApJ, 791, 130
Zavala J. A. et al., 2025, Nat. Astron., 9, 155
Zitrin A. et al., 2015, ApJ, 810, L12

APPENDIX A: EMISSION-LINE FITTING

When fitting the emission lines, we fix the emission-line widths using the LSF derived in Stefanon et al. (in preparation) and the line centroids according to the [C II] redshift, accounting for a small wavelength offset in the NIRSpec observations, as detailed in Stefanon et al. (in preparation). We show the emission line-fitted, continuum-subtracted integrated spectrum and residuals for each galaxy in Figs A1 and A2.

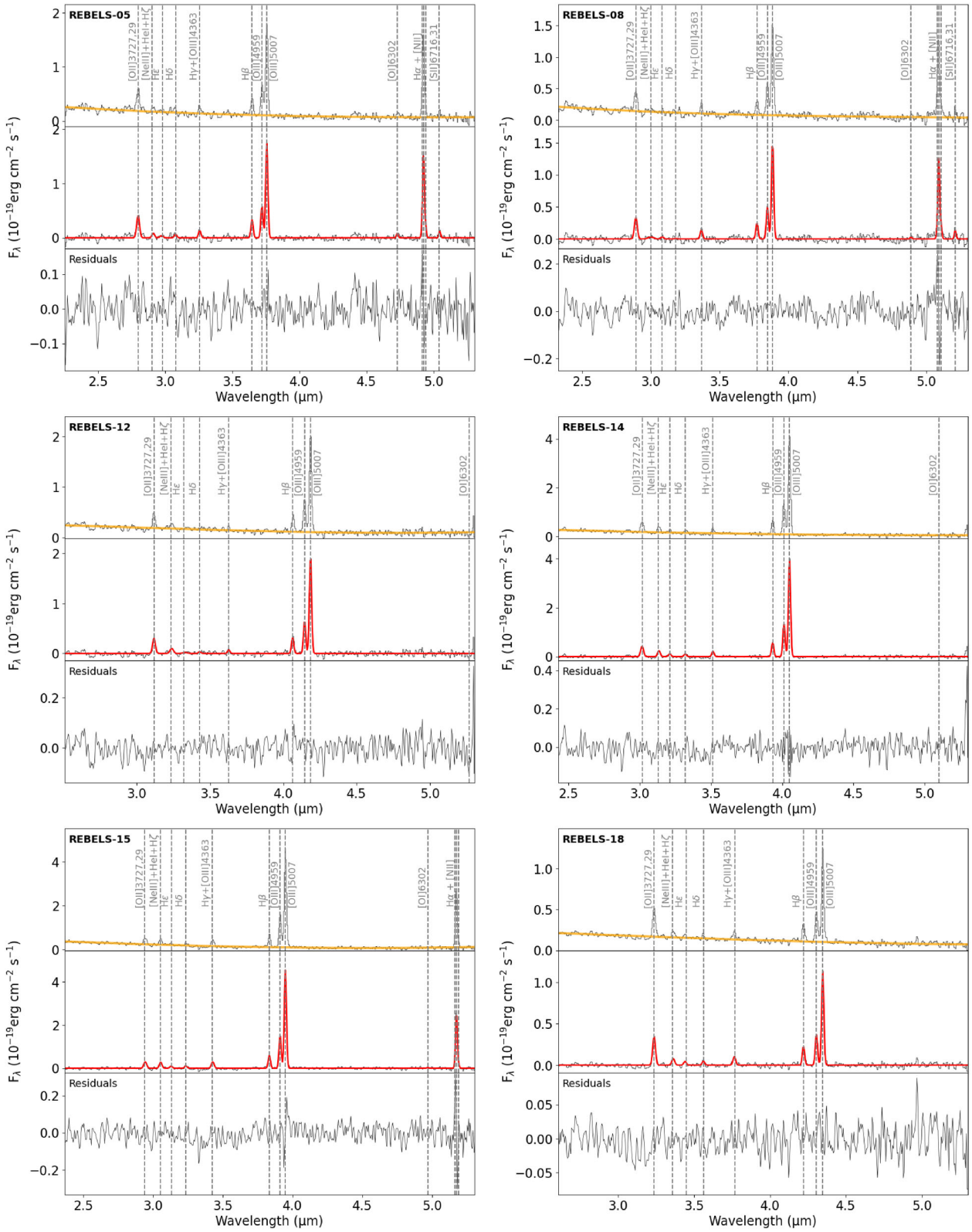

Figure A1. For each subfigure, we show a portion (rest-frame wavelength > 0.3 μm) of the observed spectrum of each galaxy (labelled in the top-left corner) which covers the key rest-frame optical nebular emission lines studied in this paper. For each galaxy, we plot the observed spectrum in grey and the PYSPECKIT continuum fit in orange in the top panel. In the middle panel, the Gaussian fits to each emission line in the continuum-subtracted spectrum are plotted in red, and in the bottom panel, we plot the residuals of our emission-line fitting.

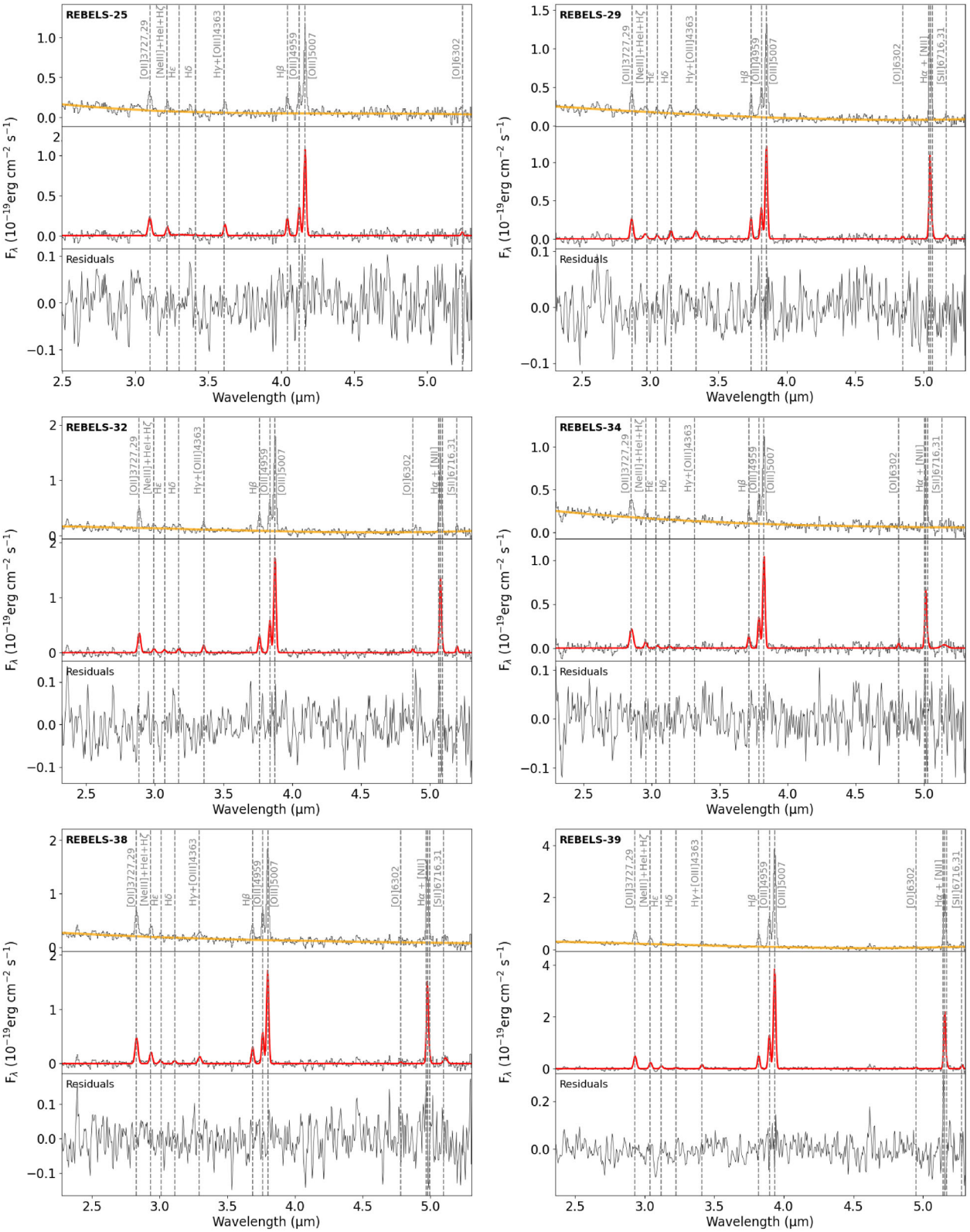

Figure A2. As with Fig. A1.

APPENDIX B: BALMER DECREMENTS

For 8/12 of the REBELS galaxies, we have the wavelength coverage to detect Hα emission. For six of these, we detect Hγ+[O III]λ4363 emission at $> 3\sigma$. Assuming that the contribution of the auroral [O III]λ4363 line to this emission is negligible in comparison to the uncertainties, we compare the $A_{V,\,neb}$ determined from the Hα/Hβ ratio to that from the Hγ/Hβ ratio, using an intrinsic ratio of 0.47 for

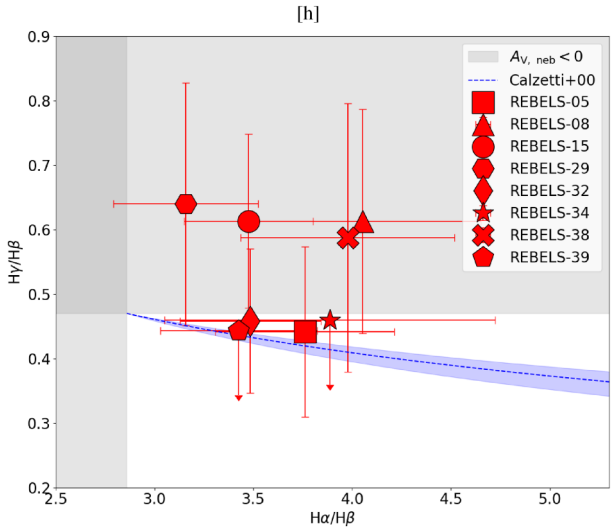

Figure B1. For 8/12 targets, we have the wavelength coverage for Hα, Hβ, and Hγ. We plot a comparison of the Hγ/Hβ and Hα/Hβ Balmer decrements for these eight sources, and compare to the expected trend assuming D. Calzetti et al. (2000) dust attenuation with theoretical values of Hγ/Hβ = 0.47 and Hα/Hβ = 2.86. The Hγ/Hβ ratios of these REBELS galaxies are consistent with unphysical values (assuming Case B recombination) of the nebular attenuation (shown with the grey shading), likely due to the low SNR of Hγ. We therefore do not use the Hγ/Hβ to attenuation-correct the line fluxes of the four sources where Hα falls outside of our wavelength coverage, and we instead report their attenuation-uncorrected fluxes in Table 3.

Hγ/Hβ (also following Case B recombination, D. E. Osterbrock & G. J. Ferland 2006). The derived $A_{V,\ neb}$ are consistent within the uncertainties for four of these six galaxies, however we find that the Hγ/Hβ ratios are consistent with unphysical values (assuming Case B recombination) within the 1σ uncertainties for all six (Fig. B1). This could be due to a non-negligible contribution from [O III]λ4363 emission (and/or [Fe II]λ4360, which dominates over the auroral line in metal-rich galaxies, M. Curti et al. 2017; A. E. Shapley et al. 2025), causing the Hγ/Hβ to be greater than 0.47, or due to the low SNR of these detections. Similarly, other studies have also found sources which appear to deviate from Case B recombination (e.g. N. Pirzkal et al. 2024; C. Scarlata et al. 2024). Due to these uncertainties with using the Hγ/Hβ ratio to determine the attenuation, we do not attempt a reddening correction of the emission-line fluxes based on the Balmer decrement for the four galaxies at $z \gtrsim 7$, where Hα is beyond the wavelength coverage of NIRSpec. We therefore give their non-attenuation-corrected values in Table 3.

APPENDIX C: METALLICITY ESTIMATES WITH DIFFERENT CALIBRATIONS

Due to the considerable discrepancies found between different strong-line indices and calibrations used to derive oxygen abundances in the literature, we rederive the oxygen abundances of the REBELS sample using a variety of different calibrations, which we list in Tables C1–C4. For the K. Nakajima et al. (2022) calibrations, we show results from both the high equivalent width (EW$>$ 200Å) calibrations (calibrated for 12 + log(O/H) $\sim$ 7.1–8.1), and the calibrations based on the sample including stacked SDSS galaxies at higher metallicities (calibrated for 12 + log(O/H) $\sim$ 7.0–8.9) collected therein. Although some of our Hβ EWs are $<$ 100 Å, our observed R23, R3, and O32 ratios are above the cut-off of the small-

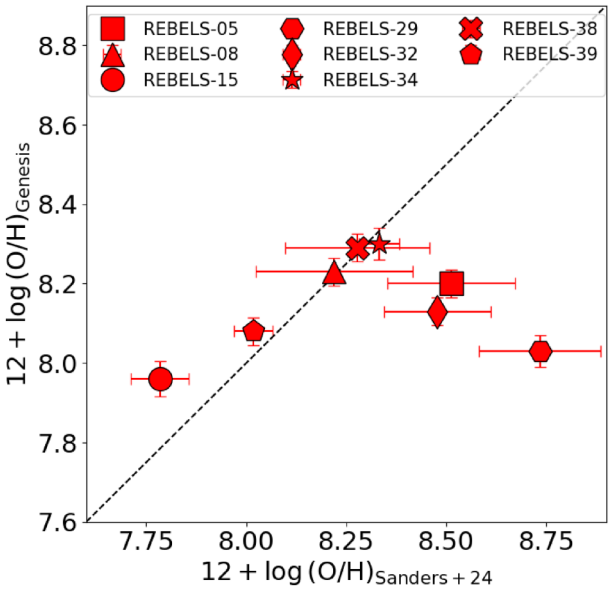

Figure C1. A comparison between the fiducial metallicity estimates using the empirically derived calibrations in R. L. Sanders et al. (2024) with metallicity estimates using the non-parametric `genesis` method (D. Langeroodi & J. Hjorth 2024).

EW calibration range, and the medium EW calibrations are not well behaved due to the small sample size. Similarly, in I. H. Laseter et al. (2024), the sample show higher ionization and excitation ratios at a given metallicity than local galaxies with rest-frame Hβ EW= 200–300 Å, but have $\sim 2\times$ lower EWs, implying that Hβ EW may not be a good probe of excitation conditions at this redshift, when making comparisons to lower redshifts.

We also used the calibration derived in I. H. Laseter et al. (2024), which uses $\hat{R} = 0.47 \log_{10} R2 + 0.88 \log_{10} R3$. However, we obtain real solutions for only two galaxies with attenuation-corrected fluxes in the REBELS sample, which are for REBELS-15 and REBELS-29. For REBELS-15, the two solutions with the $\hat{R}$ calibration are 7.95 and 8.27, and for REBELS-29 they are 7.79 and 8.39.

In Fig. 5, we compared some observed emission-line ratios with those in the `HII-CHI-Mistry` models. As discussed in Section 4.1, these models can also be used to constrain the ionization parameter and, in addition, the oxygen abundance. For these fits, we input all the observed reddening-corrected emission lines (excluding the Balmer lines) relative to Hβ from Table 2. The resulting oxygen abundances range from 12 + log(O/H) = 8.0 to 8.3, and are all consistent within the uncertainties with the oxygen abundances derived using Ne3O2, O32, and O2 ratios from Tables C1 and C3.

In addition, we use the non-parametric gas-phase metallicity estimator, `genesis` (D. Langeroodi & J. Hjorth 2024) for the 8/12 galaxies where Hα is detected. `genesis` uses inputted R3, R2, and EW(Hβ) values to estimate the oxygen abundance, and is calibrated on a sample of 1551 [OIII]λ4363 detections at $0 < z < 10$, although $>$ 75 per cent are at $z \lesssim 1$. This sample includes the galaxies in each of the calibration samples of the aforementioned metallicity calibration papers. We plot the comparison between the fiducial oxygen abundances derived from the R. L. Sanders et al. (2024) calibrations with those estimated with `genesis` in Fig. C1. We find that these metallicity estimates very closely align with the R. L. Sanders et al. (2024) O32 and O2 estimates in Table C1.

From this sample of galaxies, it is clear that there are significant offsets, by as much as $\sim$ 0.6 dex, between different commonly used

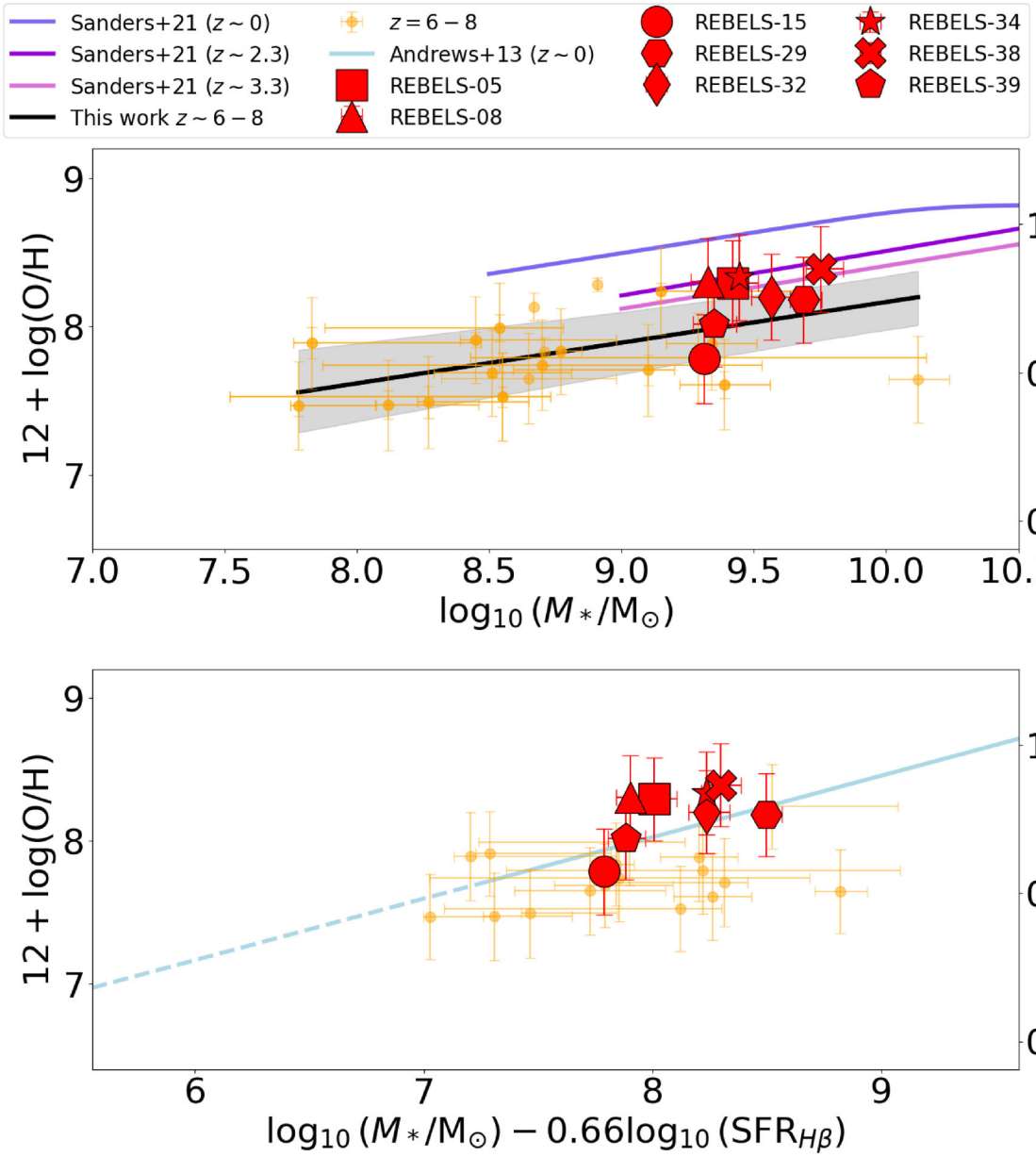

Figure C2. We plot the MZR (top panel) and FMR (lower panel) for the sources where the attenuation-corrected O32 ratio can be used to determine the metallicity. Markers, lines, and shading are the same as in Figs 6 and 7.

Table C1. Oxygen abundances derived from various strong-line indices using the R. L. Sanders et al. (2024) calibrations. Missing values indicate either undetected emission lines, or no real solutions to the calibration.

Galaxy	O3	R23	Ne3O2	O32	O2
REBELS-05	8.44 ± 0.14	8.51 ± 0.16	–	8.29 ± 0.29	8.23 ± 0.23
REBELS-08	8.29 ± 0.17	8.22 ± 0.22	–	8.31 ± 0.29	8.30 ± 0.23
REBELS-12	8.23 ± 0.13	–	8 ± 0.28	–	–
REBELS-14	7.90 ± 0.12	–	7.89 ± 0.25	–	–
REBELS-15	–	–	7.67 ± 0.27	7.78 ± 0.30	7.84 ± 0.24
REBELS-18	8.50 ± 0.13	–	8.24 ± 0.27	–	–
REBELS-25	8.62 ± 0.17	–	8.02 ± 0.27	–	–
REBELS-29	8.57 ± 0.14	8.73 ± 0.15	–	8.18 ± 0.29	8.06 ± 0.23
REBELS-32	8.38 ± 0.13	8.48 ± 0.13	–	8.20 ± 0.29	8.16 ± 0.23
REBELS-34	–	–	–	8.33 ± 0.29	8.43 ± 0.24
REBELS-38	8.38 ± 0.16	8.28 ± 0.18	8.01 ± 0.26	8.39 ± 0.29	8.36 ± 0.23
REBELS-39	–	–	7.95 ± 0.26	8.02 ± 0.29	8.09 ± 0.23

Table C2. Oxygen abundances derived from various strong-line indices using the K. Nakajima et al. (2022) calibrations for the high EW, local analogue sample, calibrated for $12 + \log(O/H) \sim 7.1 - 8.1$. Missing values indicate either undetected emission lines, or no real solutions to the calibration.

Galaxy	O3	R23	Ne3O2	O32	O2	N2	O3N2
REBELS-05	8.54 ± 0.19	8.51 ± 0.15	–	8.43 ± 0.39	8.38 ± 0.37	9.19 ± 0.26	9.07 ± 0.49
REBELS-08	8.40 ± 0.2	8.21 ± 0.17	–	8.44 ± 0.40	8.45 ± 0.40	9.32 ± 0.26	9.1 ± 0.48
REBELS-12	8.35 ± 0.18	–	8.18 ± 0.42	–	–	–	–
REBELS-14	8.15 ± 0.17	–	8.08 ± 0.40	–	–	–	–
REBELS-15	–	–	7.84 ± 0.41	7.94 ± 0.40	7.99 ± 0.43	–	–
REBELS-18	8.60 ± 0.18	–	8.35 ± 0.42	–	–	–	–
REBELS-25	8.71 ± 0.20	–	8.20 ± 0.42	–	–	–	–
REBELS-29	8.66 ± 0.19	8.71 ± 0.15	–	8.35 ± 0.39	8.22 ± 0.36	9.26 ± 0.26	9.14 ± 0.48
REBELS-32	8.48 ± 0.18	8.48 ± 0.14	–	8.36 ± 0.39	8.32 ± 0.34	8.95 ± 0.28	8.91 ± 0.53
REBELS-34	–	–	–	8.46 ± 0.40	8.55 ± 0.48	–	–
REBELS-38	8.48 ± 0.19	8.28 ± 0.16	8.19 ± 0.4	8.5 ± 0.39	8.5 ± 0.37	9.08 ± 0.28	8.99 ± 0.52
REBELS-39	–	–	8.14 ± 0.41	8.21 ± 0.40	8.25 ± 0.38	–	–

Table C3. Oxygen abundances derived from various strong-line indices using the K. Nakajima et al. (2022) calibrations for the full sample, including stacked SDSS spectra at higher metalliities (range of $6.9 < 12 + \log(O/H) < 8.9$ for all but Ne3O2, which has range $7 < 12 + \log(O/H) < 8.1$). Missing values indicate either undetected emission lines, or no real solutions to the calibration.

Galaxy	R3	R23	Ne3O2	O32	O2	N2	O3N2
REBELS-05	8.15 ± 0.17	8.17 ± 0.18	–	8.18 ± 0.39	8.26 ± 0.27	8.45 ± 0.24	9.03 ± 0.42
REBELS-08	8.02 ± 0.22	–	–	8.19 ± 0.39	8.34 ± 0.28	8.50 ± 0.24	9.02 ± 0.42
REBELS-12	–	–	–	–	–	–	–
REBELS-14	–	–	8.93 ± 0.58	–	–	–	–
REBELS-15	–	–	9.78 ± 0.61	–	7.78 ± 0.27	–	–
REBELS-18	8.19 ± 0.17	–	–	–	–	–	–
REBELS-25	8.26 ± 0.17	–	–	–	–	–	–
REBELS-29	8.23 ± 0.17	8.36 ± 0.13	–	8.09 ± 0.39	8.07 ± 0.27	8.48 ± 0.24	9.01 ± 0.42
REBELS-32	8.10 ± 0.17	8.12 ± 0.19	–	8.10 ± 0.39	8.18 ± 0.27	8.36 ± 0.24	9.06 ± 0.42
REBELS-34	–	–	–	8.21 ± 0.39	–	–	–
REBELS-38	8.11 ± 0.18	–	–	8.25 ± 0.39	8.42 ± 0.28	8.41 ± 0.24	9.04 ± 0.42
REBELS-39	–	–	–	7.91 ± 0.40	8.11 ± 0.27	–	–

Table C4. Oxygen abundances derived from various strong-line indices using the F. Bian et al. (2018) calibrations. Missing values indicate either undetected emission lines, or no real solutions to the calibration. We note that the reported uncertainties are only based on the propoagated uncertainties in the fluxes, since the uncertainty in the calibrations is not given in F. Bian et al. (2018).

Galaxy	R3	R23	Ne3O2	O32	N2	O3N2
REBELS-05	–	–	–	8.31 ± 0.027	8.42 ± 0.049	8.3 ± 0.049
REBELS-08	–	–	–	8.32 ± 0.03	8.49 ± 0.043	8.32 ± 0.043
REBELS-12	–	–	8.04 ± 0.085	–	–	–
REBELS-14	–	–	7.97 ± 0.041	–	–	–
REBELS-15	–	–	7.84 ± 0.071	7.97 ± 0.05	–	–
REBELS-18	–	–	8.19 ± 0.082	–	–	–
REBELS-25	–	–	8.06 ± 0.078	–	–	–
REBELS-29	–	–	–	8.24 ± 0.027	8.45 ± 0.048	8.34 ± 0.048
REBELS-32	–	–	–	8.25 ± 0.02	8.29 ± 0.069	8.21 ± 0.069
REBELS-34	–	–	–	8.34 ± 0.034	–	–
REBELS-38	–	–	8.05 ± 0.054	8.38 ± 0.024	8.36 ± 0.064	8.25 ± 0.064
REBELS-39	–	–	8.01 ± 0.069	8.13 ± 0.033	–	–

strong-line metallicity calibrations. However, when re-analysing the MZR and FMR with R3, R23, and O32 indices across the various calibrations, we find that the choice of calibration has little effect on the slope, intercept, or scatter of these relations. For example, we show in Fig. C2, the MZR using only the galaxies with attenuation-corrected O32 ratios and using the O32 metallicity calibration from R. L. Sanders et al. (2024). By fitting the MZR according to equation (9), we find a slope $\gamma = 0.27 \pm 0.07$ and an intercept $Z_{10} = 8.17 \pm 0.08$, which is consistent within the uncertainties with the values reported in Section 6.1.

[1]*Leiden Observatory, Leiden University, PO Box 9513, NL-2300 RA Leiden, The Netherlands*
[2]*Departament d'Astronomia i Astrofísica, Universitat de València, C. Dr Moliner 50, E-46100 Burjassot, València, Spain*
[3]*Unidad Asociada CSIC 'Grupo de Astrofísica Extragaláctica y Cosmología' (Instituto de Física de Cantabria, Universitat de València), Spain*
[4]*Institute of Astronomy and Astrophysics, Academia Sinica, 11F of Astronomy-Mathematics Building, No.1, Section 4, Roosevelt Rd, Taipei 106216, Taiwan, ROC*
[5]*Hiroshima Astrophysical Science Center, Hiroshima University, 1-3-1 Kagamiyama, Higashi-Hiroshima, Hiroshima 739-8526, Japan*
[6]*National Astronomical Observatory of Japan, 2-21-1, Osawa, Mitaka, Tokyo, Japan*
[7]*Jodrell Bank Centre for Astrophysics, Department of Physics and Astronomy, School of Natural Sciences, The University of Manchester, Manchester M13 9PL, UK*
[8]*Canadian Institute for Theoretical Astrophysics, 60 St George St, University of Toronto, Toronto, ON M5S 3H8, Canada*
[9]*David A. Dunlap Department of Astronomy and Astrophysics, University of Toronto, 50 St George St, Toronto ON M5S 3H8, Canada*
[10]*Department of Physics, 60 St George St, University of Toronto, Toronto, ON M5S 3H8, Canada*
[11]*Kapteyn Astronomical Institute, University of Groningen, NL-9700 AV Groningen, The Netherlands*
[12]*Scuola Normale Superiore, Piazza dei Cavalieri 7, I-56126 Pisa, Italy*
[13]*Dipartimento di Fisica 'Enrico Fermi', Universitá di Pisa, Largo Bruno Pontecorvo 3, Pisa I-56127, Italy*
[14]*Department of Astronomy, University of California, Berkeley, Berkeley, CA 94720, USA*
[15]*Cosmic Dawn Center (DAWN), Jagtvej 128, DK-2200 N, Copenhagen, Denmark*
[16]*Niels Bohr Institute, University of Copenhagen, Jagtvej 128, DK-2200 Copenhagen N, Denmark*
[17]*Department of Astronomy, University of Geneva, Chemin Pegasi 51, CH-1290 Versoix, Switzerland*
[18]*Instituto de Estudios Astrofícos, Facultad de Ingeniería y Ciencias, Universidad Diego Portales, Av. Ejército 441, Santiago, Chile*
[19]*Millenium Nucleus for Galaxies (MINGAL), Av. Ejército 441, Santiago 8370191, Chile*
[20]*Department of Astronomy, University of Texas, Austin, TX 78712, USA*
[21]*Center for Frontier Science, Chiba University, 1-33 Yayoi-cho, Inage-ku, Chiba 263-8522, Japan*
[22]*Departmento de Astronomia, Universidad de Chile, Casilla 36-D, Santiago 7591245, Chile*
[23]*Dipartimento di Fisica, Sapienza, Università di Roma, Piazzale Aldo Moro 5, I-00185 Roma, Italy*
[24]*INFN, Sezione di Roma I, Piazzale Aldo Moro 2, I-00185 Roma, Italy*
[25]*INAF/Osservatorio Astrofisico di Arcetri, Largo E. Femi 5, I-50125 Firenze, Italy*
[26]*Department of Astronomy, the Pennsylvania State University, 525 Davey Lab, University Park, PA 16802*
[27]*Sterrenkundig Observatorium, Ghent University, Krijgslaan 281-S9, B-9000 Ghent, Belgium*
[28]*Centre for Astrophysics and Supercomputing, Swinburne University of Technology, P.O. Box 218, Hawthorn, VIC 3122, Australia*
[29]*Astrophysics Research Institute, Liverpool John Moores University, 146 Brownlow Hill, Liverpool L3 5RF, UK*
[30]*Dipartimento di Fisica e Astronomia 'Augusto Righi', Alma Mater Studiorum, Università di Bologna, Via Gobetti 93/2, I-40129 Bologna, Italy*
[31]*INAF, Osservatorio di Astrofisica e Scienza dello Spazio, Via Gobetti 93/3, I-40129 Bologna, Italy*
[32]*Center for Computational Astrophysics, Flatiron Institute, 162 5th Avenue, New York, NY 10010, USA*
[33]*Department of Astronomy, University of Massachusetts, Amherst, MA 01003, USA*

This paper has been typeset from a TEX/LATEX file prepared by the author.